

Weak correlations between hemodynamic signals and ongoing neural activity during the resting state

Aaron T. Winder^{1,2}, Christina Echagarruga^{1,3}, Qingguang Zhang^{1,2} and Patrick J. Drew^{1,2,3,4*}

Spontaneous fluctuations in hemodynamic signals in the absence of a task or overt stimulation are used to infer neural activity. We tested this coupling by simultaneously measuring neural activity and changes in cerebral blood volume (CBV) in the somatosensory cortex of awake, head-fixed mice during periods of true rest and during whisker stimulation and volitional whisking. We found that neurovascular coupling was similar across states and that large, spontaneous CBV changes in the absence of sensory input were driven by volitional whisker and body movements. Hemodynamic signals during periods of rest were weakly correlated with neural activity. Spontaneous fluctuations in CBV and vessel diameter persisted when local neural spiking and glutamatergic input were blocked, as well as during blockade of noradrenergic receptors, suggesting a non-neuronal origin for spontaneous CBV fluctuations. Spontaneous hemodynamic signals reflect a combination of behavior, local neural activity, and putatively non-neural processes.

Spontaneous hemodynamic signals are extensively used in resting-state functional MRI (fMRI) studies to infer neural activity not driven by tasks or stimuli^{1,2}. A cornerstone assumption of these studies is that spontaneous hemodynamic signals are coupled to neural activity in the same manner as hemodynamic signals elicited by sensory stimuli. Recent studies have cast doubt on the one-to-one coupling of neural activity to hemodynamic signals during sensory stimulation^{3–5}, making it critical to determine how spontaneous hemodynamic signals are coupled to neural activity. To determine what aspects of neural activity are reported by spontaneous hemodynamic signals during different states, we simultaneously measured neural activity⁶ and CBV using intrinsic optical imaging^{4–6} in the vibrissal cortex of awake, head-fixed mice^{7,8} (Fig. 1a,c and Supplementary Fig. 1a) while monitoring whisker and body movements. Increases in CBV, which show up as decreases in reflectance in intrinsic optical imaging signals, are caused by arterial and capillary dilations^{9,10} and lead to increases in oxygenation, which can be detected with blood oxygen level-dependent (BOLD) fMRI^{11,12}. Although our optical signals originated from the superficial layers, CBV changes have similar dynamics and amplitudes throughout the depth of cortex¹³, and CBV increases are tightly related to BOLD fMRI signals¹⁴.

Results

Behavior drives spontaneous hemodynamic fluctuations

Since humans and animals continuously engage in small bodily motions^{15,16} and actively sense their environment¹⁷, we monitored body movement and whisker position to detect periods of active behavior and rest (Fig. 1f and Supplementary Fig. 1b). We obtained an average of 254 ± 54 min of simultaneous CBV, neural, and behavioral data from each mouse ($n = 12$ mice; Fig. 1b). We categorized the data into several states: stimulation of the whiskers (contralateral to the window) with brief, gentle puffs of air directed towards the whiskers but not the face⁷; volitional whisking; and rest (Fig. 1b,f and Online Methods). Periods of time greater than 10 s in duration without stimulation in which the animals did not volitionally whisk were defined as true rest. Periods of rest lasting less than 10 s were considered transitions between behaviors and were omitted from subsequent analyses. Extended (>2 s) volitional whisker movements

were analyzed separately from brief volitional movements since they were generally associated with additional body motion and distinct vascular responses¹³. We also used auditory stimulation (air puffs aimed away from the body) and stimulation of ipsilateral whiskers, but as these stimuli primarily elicited volitional whisking behavior (Supplementary Fig. 1h), we focus below on rest, volitional whisking, and stimulation of the contralateral whiskers in subsequent analyses.

We first asked whether there were any differences in the amplitude of hemodynamic fluctuations across these different states, as nonstationarities in variance have been postulated to account for most of resting-state connectivity¹⁸, though this nonstationarity has been argued to be spurious and driven by head movement and/or sampling variability¹⁹. As our signals were unaffected by head motion and as we can parse our data into identified behavioral epochs, we can directly address this issue in our system. The variance of hemodynamic signal fluctuations in our mice was significantly and substantially larger during all of these states than at rest (Fig. 1e). These results show that, in the awake brain, active sensation and volitional movements drive substantial changes in hemodynamic signals, and variability in the amount of these behaviors contributes to the large trial-to-trial variability observed in hemodynamic signals ‘at rest’²⁰. While our observation that the variance in the CBV signal differed among behavioral states does not rule out statistical or head-motion-related artifacts in generating or contaminating dynamic connectivity patterns seen in human fMRI¹⁹, it shows that the amplitude of spontaneous hemodynamic signals will be affected by behavioral state.

Correlations between spontaneous neural activity and CBV changes

We then examined what aspect of neural activity was correlated with the observed CBV changes. Electrophysiology is considerably more sensitive to low levels of neural activity than calcium imaging, which fails to detect a substantial proportion of the action potentials, particularly at low firing rates²¹, and which cannot detect local field potential (LFP) oscillations. Consistent with previous measures showing a relatively tight spatial relationship between CBV changes and neural activity⁶, we observed that the measured reflectance from pixels near the stereotrode recording site was correlated

¹Center for Neural Engineering, Pennsylvania State University, University Park, PA, USA. ²Department of Engineering Science and Mechanics, Pennsylvania State University, University Park, PA, USA. ³Graduate Program in Bioengineering, Pennsylvania State University, University Park, PA, USA. ⁴Department of Neurosurgery and Department of Biomedical Engineering, Pennsylvania State University, University Park, PA, USA. *e-mail: pjd17@psu.edu

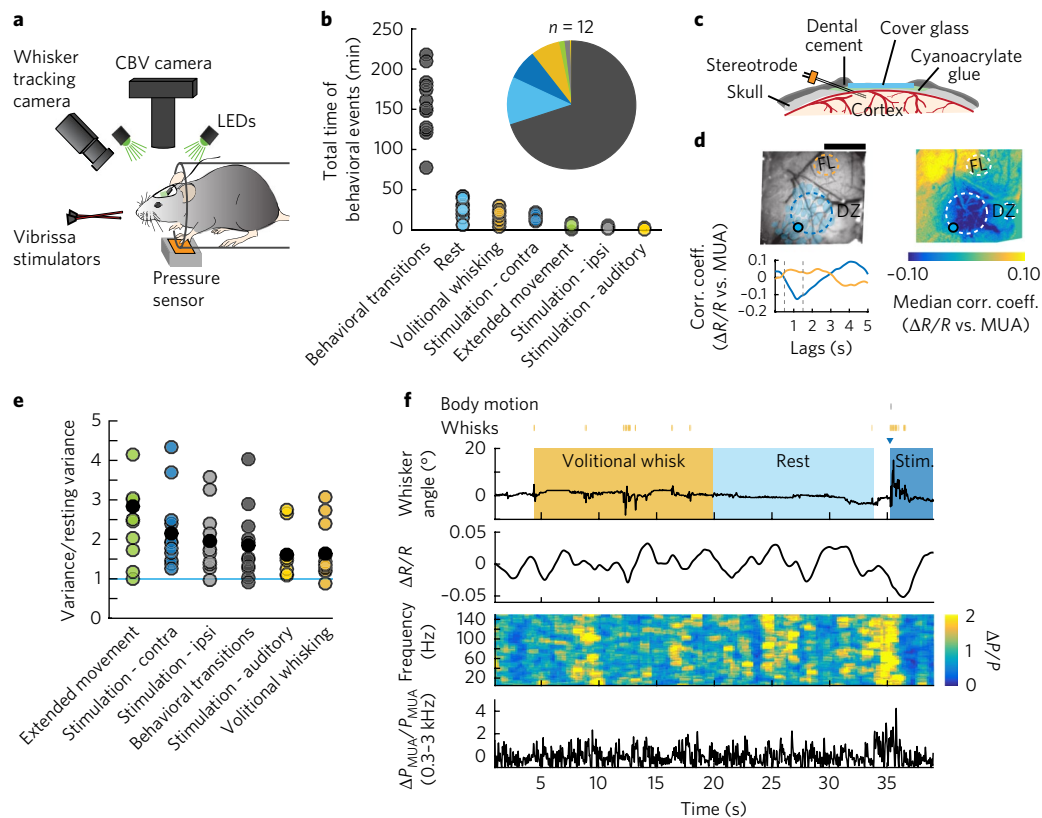


Fig. 1 | Behavior drives CBV fluctuations. **a**, Schematic of the experimental setup. **b**, Total behavioral times, in minutes, for each animal (circles, $n=12$ mice). Inset: the median portion of recorded data corresponding to each behavior. **c**, Schematic of the reinforced thinned-skull windows and implanted stereotrode. **d**, Representative example from a single animal showing that correlations between CBV (changes in reflectance, $-\Delta R/R$) and neural activity were largest near the stereotrode for all animals ($n=12$ mice). Top left: image of a thinned skull window. Filled circle indicates the reconstructed location of the stereotrode tip. Blue shaded regions show the location of whisker barrels. Dashed circular regions designate the locations of ROIs. FL, forelimb; DZ, dysgranular zone. Scale bar, 1 mm. Top right: the pixel-wise correlation coefficients between multiunit power (300–3,000 Hz) and $\Delta R/R$ during rest for the representative animal. Colors denote the median correlation coefficient for MUA lag times of 0.5–1.5 s (dashed vertical lines, below). Bottom left: cross-correlations between multiunit power and each of the anatomically determined ROIs. Positive lags indicate that CBV follows neural activity. Dashed lines indicate the period over which the median correlation coefficient was calculated in the pixel-wise map. **e**, The variance in CBV for each state, normalized by the CBV variance during rest. Each circle represents data from single mouse ($n=12$). All behaviors show CBV variances significantly larger than resting variance. (Wilcoxon signed-rank test, Bonferroni corrected, extended movement: $P=0.01$, $z=3.06$; contralateral stimulation: $P=0.01$, $z=3.06$; ipsilateral stimulation: $P=0.02$, $z=2.98$; behavioral transitions: $P=0.02$, $z=2.98$; auditory stimulation: $P=0.05$, $z=2.67$; volitional whisking: $P=0.02$, $z=2.90$). Contra, contralateral; ipsi, ipsilateral. **f**, Example of data from a single trial. Top: periods of volitional whisking (orange), sensory stimulation (dark blue), and rest (light blue). Vibrissa stimulation is denoted by the dark blue triangle and volitional whisks or body movements as orange or gray tick marks, respectively. Second from top: normalized CBV changes ($\Delta R/R$) were measured by averaging the reflectance within the region of interest in the vibrissal cortex. Second from bottom: normalized neural power ($\Delta P/P$) was calculated between 5 and 150 Hz. Bottom: MUA power was summed between 300 and 3,000 Hz.

to the multiunit average (MUA, a measure of local spiking) during periods of rest in all animals (Fig. 1d). Passive sensory stimulation and volitional whisking both evoked increases in gamma-band power (40–100 Hz) of the LFP and in low-frequency power (<5 Hz) of the LFP, MUA, and CBV (Fig. 2a,b), similarly to responses in the visual system of primates^{4,22}; however, the MUA response to whisker stimulation and volitional whisking varied among animals²³. The heart-rate increase induced by the sensory stimulus was small ($2.2 \pm 1.3\%$; Supplementary Fig. 2c,e), and the CBV responses were localized to the histologically reconstructed vibrissal cortex and the adjacent multisensory area²⁴ (Supplementary Fig. 11). The sensory-evoked CBV increase was not altered in mice with facial nerve transections, which prevented whisking (Supplementary Fig. 3a), showing that stimulus-elicited whisking had a negligible effect on the sensory-evoked CBV response²⁵. During periods of rest, power increases in the gamma band²⁰ and the MUA were consistently correlated with CBV increases (Fig. 2c and Supplementary Fig. 4). The correlations between neural activity and CBV in the absence of

sensory stimulation were not substantially affected by facial motor nerve transection (Supplementary Fig. 3b,c), demonstrating that these spontaneous fluctuations in neural activity were centrally generated and were not reafferent signals.

Neurovascular coupling was similar across behavioral states

We first tested whether neurovascular coupling was similar across different states (sensory stimulation, volitional whisking, and rest). To quantitatively compare the relationship between neural activity and CBV, we calculated the hemodynamic response function (HRF)^{4,9,26}, which is the kernel that relates neural activity to subsequent changes in blood volume. We selected a region of interest (ROI) around the electrode (mean area \pm s.d.: 0.6 ± 0.1 mm²) based on the resting CBV–MUA correlation map and location of vibrissal cortex (Fig. 1d and Online Methods) to maximize the likelihood of obtaining a strong correlation between neural activity and CBV during rest. We compared HRFs calculated from neural and hemodynamic data, segregated by behavioral state, to determine whether behavior modulated the relationship

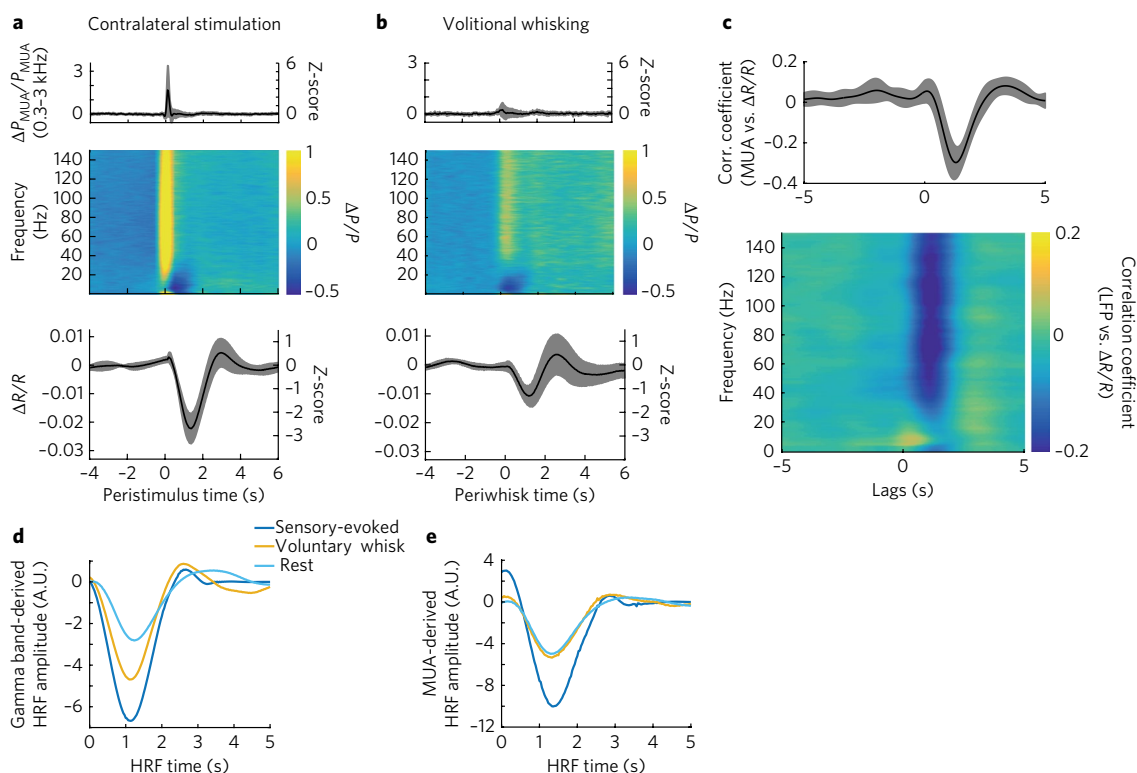


Fig. 2 | Neurovascular coupling was consistent across behavioral states. **a**, Average population ($n=12$ animals) responses to contralateral whisker stimulation. Top: average normalized stimulus-evoked changes in MUA power. Middle: average normalized stimulus-evoked changes in LFP power as a function of frequency. Bottom: reflectance change ($\Delta R/R$) within the vibrissal ROI. **b**, Average population ($n=12$ animals) responses to voluntary whisker movement. Plots are as in **a**. Shaded areas indicate the population s.d. **c**, Mean cross-correlations between neural activity and $\Delta R/R$ calculated during periods of rest show that MUA power (top) and gamma-band power (bottom; 40–100 Hz) were reliably correlated with CBV changes. The shaded regions denote ± 1 s.d. ($n=12$ animals). **CBV increases lagged neural activity changes by 1.3 ± 0.14 s.** **d**, A comparison of the mean gamma-band derived HRFs. Each HRF was calculated from a single behavioral state—stimulation (sensory-evoked, dark blue), volitional whisking (orange), and rest (light blue)—and averaged across animals ($n=12$). See Supplementary Fig. 5 for individual data. **e**, As in **d** but for HRFs calculated from MUA.

between neural activity and subsequent changes in CBV. Because both sensory-evoked and spontaneous increases in CBV were most strongly and consistently correlated with gamma-band and MUA power during rest²⁰ (Fig. 2c and Supplementary Fig. 4), we focused our analysis on these neural measures. Across all states, the HRFs showed that increases in gamma-band power and MUA drove a decrease in reflectance (increases in CBV) with similar latency (Fig. 2d,e and Supplementary Fig. 5a,b), indicating that the temporal dynamics of the hemodynamic response was not different across behavioral states. The similarity of overall dynamics (time to peak, full width at half maximum) for all conditions implies that neurovascular coupling was constant across behaviors. The shapes of the HRFs were similar regardless of electrode depth (Supplementary Figs. 1g and 5c,d).

Predicting the hemodynamic response from neural activity

We then asked how well the CBV signal could be predicted using neural activity for each type of behavior, which bears on the ‘decoding’ of fMRI signals²⁷. By neural activity, we mean the electrical activity of neurons (action potentials and the summed action of excitatory and inhibitory postsynaptic potentials (EPSPs and IPSPs, respectively) that generate fluctuations in the local field potential) that generate MUA and LFP signals and which, when blocked in a brain region, perturb sensory perception²⁸ or motor behavior²⁹; we do not mean it to refer to the basal metabolic processes that reflect housekeeping functions³⁰ and that persist in the vegetative coma state. Using HRFs that correspond to each type of behavior, we predicted the stimulation-triggered or volitional-whisking-triggered average CBV

response using the stimulation-triggered or volitional-whisking-triggered average neural response, and then calculated the coefficient of determination (R^2) between the actual and predicted CBV responses⁴ (Fig. 3a,c,d, Supplementary Figs. 6 and 7a,b, and Online Methods). Because the neural and CBV signals must be time-locked to an event for averaging, this cannot be done for resting data. We observed a strong agreement between our prediction and the actual average CBV response to vibrissa stimulation using gamma-band power-derived HRFs (median \pm interquartile range: $R^2=0.77 \pm 0.24$), which was as strong as previous measures of neurovascular coupling in the visual cortex of primates^{22,31,32}. We also observed a reasonably good agreement between predicted and actual CBV responses to volitional whisking (median \pm interquartile range: $R^2=0.21 \pm 0.25$). These HRFs were then used to predict CBV fluctuations on individual stimulation, volitional whisking, and rest trials to determine how much of the ongoing CBV could be explained by neural activity. In comparison to the averaged data, the median R^2 of the CBV prediction over individual trials was substantially lower for all behavioral conditions when predicting ongoing CBV changes (Fig. 3c,d). A sliding window was used to visualize time-varying differences in prediction accuracy on a second-by-second basis during an episode containing sensory stimulation, volitional whisking, and rest. This result showed that prediction accuracy was higher during periods containing large CBV fluctuations (such as would be seen during sensory stimulation or movement; Figs. 1e and 3b,c,f and Supplementary Fig. 7f,g). CBV changes predicted from gamma-band power during rest were poor predictors of the actual CBV fluctuations (mean \pm s.d.: $R^2=0.06 \pm 0.03$) and predicted significantly less CBV variance than predictions made from

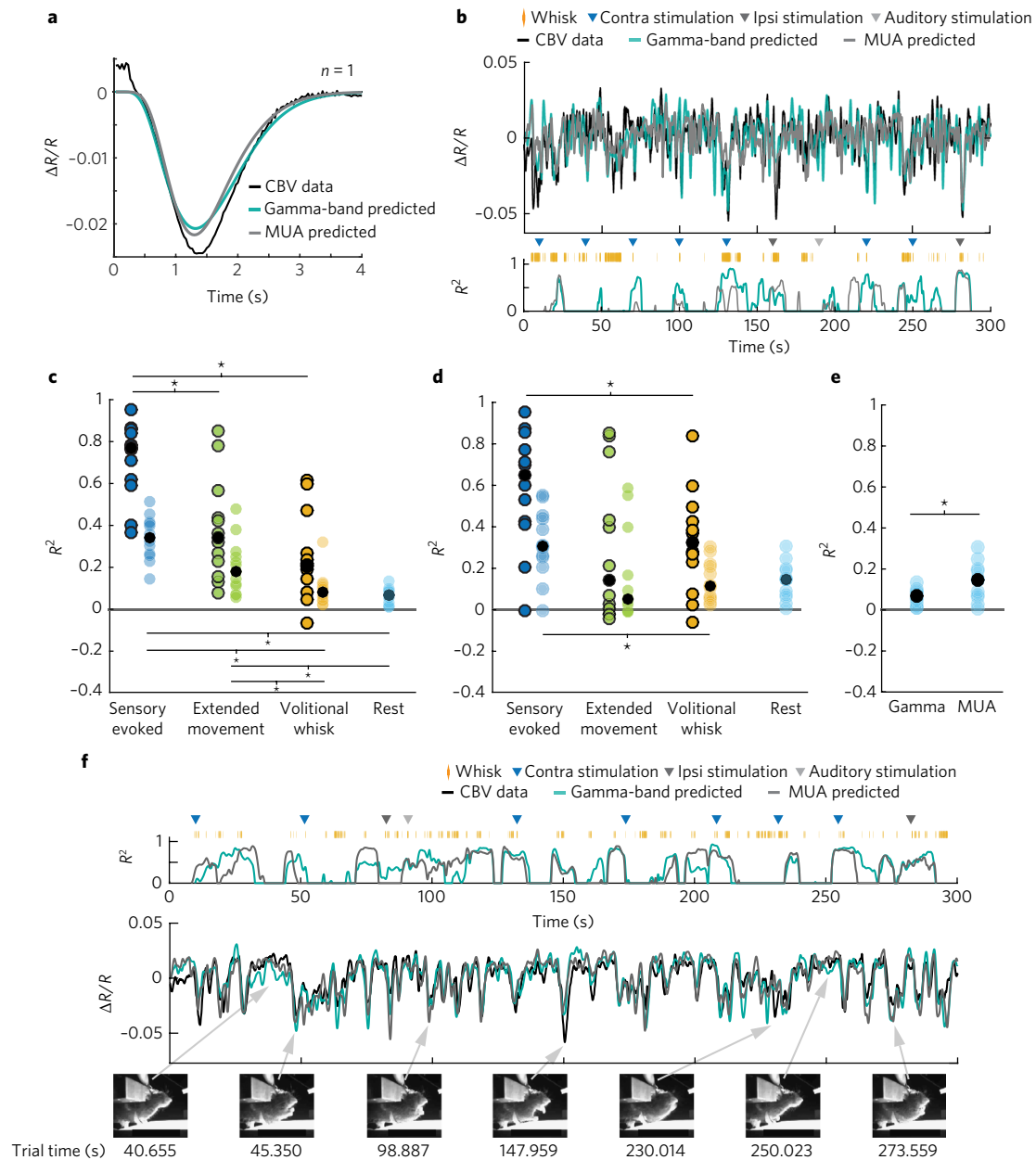


Fig. 3 | Predicting CBV changes from neural activity using HRFs. **a**, An example of the gamma-band power-derived (teal blue) and MUA-derived (gray) HRFs predicting the average stimulus-triggered CBV response (black) for a single animal. Both predictions have the same dynamics as the measured response and capture 95% of the variance (gamma-band $R^2=0.955$; MUA $R^2=0.954$). **b**, Predictions of ongoing CBV for a single trial. Top: predictions by gamma-band (teal blue, $R^2=0.29$) and MUA-derived (gray, $R^2=0.20$) HRFs. Bottom: goodness-of-fit (R^2) for 8-s sliding windows. Colored triangles indicate sensory stimuli. Orange tick marks indicate volitional whisking events. **c**, Population summary of the goodness of fit (R^2) of gamma-band power-derived CBV predictions to measured CBV, separated by behavior. Circles represent the median R^2 for each animal ($n=12$). R^2 values calculated on predictions of the average behavior-triggered CBV are outlined in black ($n=12$, two-way ANOVA, $P=8 \times 10^{-6}$, $F_{2,11}=21.02$; post hoc: paired t test, Bonferroni corrected, sensory evoked vs. extended movement: $P=1 \times 10^{-3}$, $t_{11}=4.36$; sensory evoked vs. volitional whisking: $P=6 \times 10^{-6}$, $t_{11}=8.02$; extended movement vs. volitional whisking: $P=0.14$, $t_{11}=1.57$). Colored circles without black outlines indicate the median R^2 values calculated for predictions of CBV during individual periods of behavior (Friedman test, $P=3 \times 10^{-6}$, $\chi^2_{3,33}=26.3$; post hoc: Wilcoxon signed-rank test, Bonferroni corrected, sensory evoked vs. extended movement: $P=0.11$, $z=2.35$; sensory evoked vs. volitional whisking: $P=0.02$, $z=2.98$; sensory evoked vs. rest: $P=0.01$, $z=3.06$; extended movement vs. volitional whisking: $P=0.01$, $z=3.05$; volitional whisking vs. rest: $P=0.51$, $z=1.73$; extended movement vs. rest: $P=0.02$, $z=2.98$). Filled black circles show population medians. **d**, As in **c** but for MUA-derived HRFs (averaged CBV: Friedman test, $P=0.02$, $\chi^2_{2,22}=8.17$; post hoc: Wilcoxon signed-rank test, Bonferroni corrected, sensory-evoked vs. extended movement: $P=0.045$, $z=2.43$; sensory evoked vs. volitional whisking: $P=0.02$, $z=2.67$; extended movement vs. volitional whisking: $P=0.64$, $z=-0.47$; individual CBV: Friedman test, $P=8 \times 10^{-3}$, $\chi^2_{3,33}=11.8$; post hoc: Wilcoxon signed-rank test, Bonferroni corrected, sensory evoked vs. extended movement: $P=0.25$, $z=2.04$; sensory evoked vs. volitional whisk: $P=0.03$, $z=2.82$; sensory evoked vs. rest: $P=0.09$, $z=2.43$; extended movement vs. volitional whisk: $P=0.94$, $z=-0.08$; extended movement vs. rest: $P=0.88$, $z=-0.16$; volitional whisk vs. rest: $P=0.93$, $z=0.08$, $n=12$). **e**, The MUA-derived HRF was better at predicting resting CBV fluctuations than the gamma-band power derived HRF (paired t test, $P=0.02$, $t_{11}=-2.68$). **f**, An example illustrating that ongoing animal behavior, in this case grooming, can lead to very good prediction of measured CBV. Compare to **b**; gamma-band-power-derived prediction (teal blue): $R^2=0.48$, MUA-derived prediction (gray): $R^2=0.43$. Video frames showing periods of animal behavior and rest are displayed below the data. Arrows point to the data corresponding to the video frame.

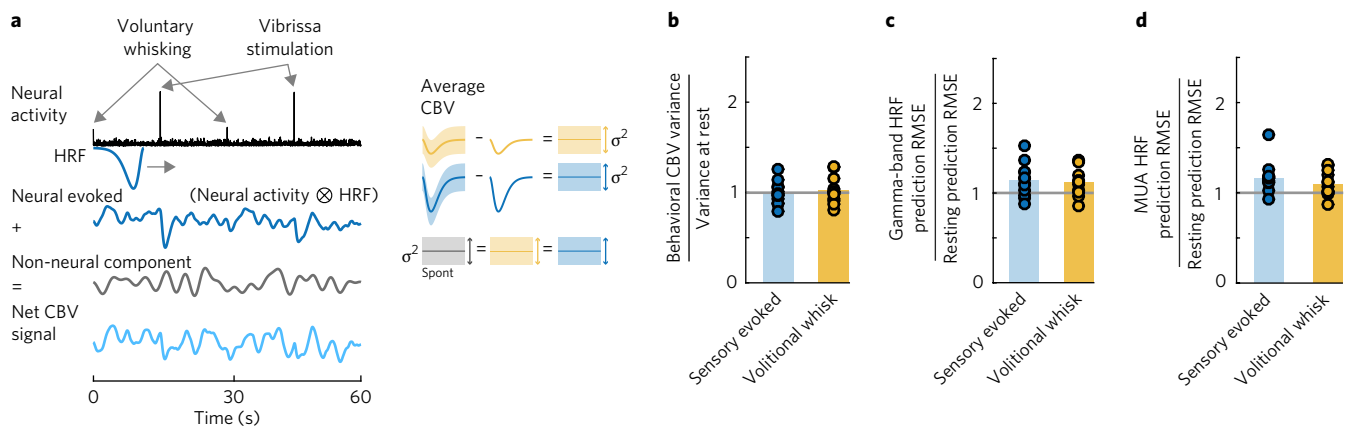


Fig. 4 | Variance of residual signal is similar across behavioral states. **a**, Top: voluntary whisking causes moderate increases in neural activity above background, while vibrissa stimulation causes large increases in neural activity. The HRF is convolved with the neural activity to give the neurally evoked component of the CBV signal. Bottom: schematic illustrating the hypothesis that the measured hemodynamic signal (Neural activity \otimes HRF) is comprised of a neurally evoked CBV component (top left, dark blue) and a separate, additive CBV component that is uncorrelated with the measured local neural activity (middle left, gray). The neurally evoked CBV component can be subtracted out using the mean response from a given behavior (top right, middle right). The variance of the residuals after subtracting the neurally driven CBV component will then be equal to the variance of the additive CBV component (bottom right). **b**, Consistent with the hypothesis in **a**, the variance in the mean CBV response after subtraction of the mean-evoked response was not significantly different from the variance in the CBV during rest (*t* test: sensory-evoked: $P=0.86$, $t_{11}=-0.18$; whisking: $P=0.61$, $t_{11}=0.52$). Each circle represents a single animal ($n=12$); bar indicates the mean. **c**, Comparison of the root-mean-squared error (RMSE) of the gamma-band-derived HRF during stimulation and volitional whisking normalized by the RMSE during rest for all animals ($n=12$). Bars indicate the means across animals. RMSE was similar between behaviors for the gamma-band (t test, Bonferroni corrected, sensory-evoked vs. rest: $P=0.06$, $t_{11}=2.70$; sensory-evoked vs. whisk: 0.73 , $t_{11}=0.35$; volitional whisk vs. rest: $P=0.07$, $t_{11}=2.66$). **d**, As in **c** but for MUA-derived HRF predictions (Wilcoxon signed-rank test, Bonferroni corrected, sensory-evoked vs. rest: $P=0.01$, $z=2.90$; sensory-evoked vs. whisk: $P=0.18$, $z=1.33$; whisk vs. rest: $P=0.07$, $z=2.27$).

MUA during rest (mean \pm s.d.: $R^2=0.14 \pm 0.09$; Fig. 3e). The low R^2 was not due to the quality of HRFs, since the HRF captured the majority of the averaged stimulus-triggered CBV variance (Fig. 3a,c,d). Lower-frequency bands (0.1–8 Hz and 10–30 Hz) of the LFP were essentially uncorrelated with resting hemodynamic signals (median $R^2 < 0.02$ for both frequency bands; Supplementary Fig. 6). Additionally, when animals were more behaviorally active, the CBV predicted from neural activity was in good agreement with measured CBV changes (Fig. 3f). The disagreement between the predicted and actual CBV on an event-by-event basis was not due to instrumentation noise (Supplementary Fig. 1d,e), and spontaneous CBV fluctuations were not substantially correlated with fluctuations in heart rate (Supplementary Fig. 2g), ruling out a systemic cardiovascular origin³³. Lastly, subtracting off the global hemodynamic signal within the window (Supplementary Fig. 7e) did not substantially improve the quality of the prediction, indicating that the signals were not generated by global blood-volume fluctuations but rather had complicated spatiotemporal dynamics (Supplementary Movie 1). These results show that the hemodynamic response was strongly coupled to the gamma band of the LFP and the MUA when neural activity was high, regardless of the source of the neural activity, but that the correlation broke down when neural activity was low, such as during rest.

Separate, additive components within the hemodynamic signal

What could account for the much lower correlation between the predicted and actual CBV for individual events versus the average and for the poor performance of the HRF in predicting CBV fluctuations during rest? As our predictions of sensory-evoked CBV changes from neural activity were consistent with previous primate studies^{4,20,22,32} (see Discussion) and performed well during behaviors with large modulations of neural activity (Fig. 3f), it seems unlikely that the weak correlations between neural activity and CBV changes at rest could be due to our experimental conditions. We hypothesized that there are two processes underlying local CBV changes: a neuronal source that drives vasodilation when neurons are active³⁴ and a second component that is uncorrelated to

the measured local neural activity and that additively interacts with the neurally evoked CBV component (Fig. 4a). In this model, the additional CBV component would be removed by averaging over stimulus presentations, since the timing of neural events would be random with respect to the phase of these uncorrelated CBV fluctuations. This hypothesis accounts for the substantially better predictions of behavior-averaged CBV changes from neural activity compared to individual events. In addition, the larger neural responses to sensory stimulation (versus volitional whisking or rest) would increase the amplitude of the neurally evoked hemodynamic signal with respect to the putatively non-neuronal component. The increased amplitude of the neurally evoked CBV would also increase the fraction of the signal that could be predicted from neural activity and account for the differences in HRF performance in predicting CBV changes from neural activity among behaviors (Fig. 3c,d and Supplementary Fig. 7f,g).

Our hypothesis makes two testable predictions. First, the two CBV components should combine additively, so that the residuals (corresponding to the portion of CBV uncorrelated with local neural activity) of the predicted CBV should have constant amplitude across states. To test for additivity, we compared the CBV variance around the mean stimulus-evoked and whisking-evoked responses to the CBV variance at rest. We found that the CBV variance during rest was not different from the trial-to-trial variance during behavior (Fig. 4b). The same pattern held true when we subtracted the neurally evoked CBV component (predicted using either the gamma-band or MUA-derived HRFs) from the measured CBV signal for each of the behavioral conditions and calculated the variance of the residuals. The level of putatively non-neuronal noise was roughly constant across conditions, as the ratio of the residuals during sensory-evoked and volitional non-neuronal periods to those during rest (as measured by the root-mean-squared error between the predicted and actual CBV signal) was close to 1 (Fig. 4c,d). The additive noise hypothesis also predicts that CBV should be better predicted by neural activity during periods with greater modulation of spontaneous (non-experimenter-evoked) neural activity, which we also saw in our

data (Supplementary Fig. 7f–h). These analyses support the hypothesis that there are two additively interacting components of the CBV, one of which is linked tightly to the measured neural activity.

Origin of spontaneous hemodynamic fluctuations

There are several mechanisms that could give rise to the component of the CBV signal that was not predicted by our measures of neural activity. One possibility is that it could be local or distant groups of neurons whose activity is not detectable in the LFP or MUA but can elicit a vasodilatory response, which we tested below. Examining the power spectra of the predicted and actual CBV changes over the entire trial (Supplementary Fig. 7c), we saw the largest difference in the 0.1–0.3-Hz range, and the power spectrum of the HRF prediction error during periods of rest (Supplementary Fig. 7d) showed a similar peak at 0.2 Hz³⁵. The spectral power of the residual CBV indicates that it is unlikely that the spontaneous activity of astrocytes drove these additive CBV oscillations because the spontaneous calcium signals in cortical astrocytes are nearly 100 times slower than the CBV fluctuations we see here (0.1–0.3 Hz versus 0.005 Hz)³⁶. However, the CBV fluctuations could be due to intrinsic oscillations in the membrane potential (and contractility) of the smooth muscle around arterioles that additively interact with vasodilatory signals from neurons, similarly to the way intrinsic membrane oscillations can sculpt response dynamics in neurons. Vascular oscillations are a plausible mechanism for the persistent CBV changes because isolated arterioles show spontaneous fluctuations in their membrane potentials and diameters in the same frequency range that we observed in the residual of our CBV prediction³⁷. Vessel diameter is linearly related to smooth muscle membrane voltage so long as the vessel is not maximally dilated³⁸, and our stimulus-induced dilations are in this linear regime (9% peak arteriole dilation to punctate contralateral vibrissa stimulation⁷ versus >40% maximum arteriole dilation³⁹). In contrast to neurally evoked fluctuations, fluctuations of a vascular origin should persist when neural activity is silenced.

We tested whether silencing local spiking blocks spontaneous CBV fluctuations during rest by infusing muscimol into the cortex via a chronically implanted cannula. The efficacy of the muscimol infusion was monitored with a stereotrode placed 1.5 ± 0.5 mm from the cannula (Fig. 5a and Supplementary Figs. 1g and 8a). A semicircular ROI, centered on the cannula and with a radius specified by the distance between the electrode and cannula, was selected to ensure that the ROI only included silenced cortex. Since we observed clear suppression of neural activity with electrodes placed ~2 mm away, the infusion should affect all cortical layers (as the cannula was placed ~200 μ m below the surface and the mouse cortex is ~1.2 mm thick).

Muscimol infusion caused a strong decrease in the sensory-evoked and baseline MUA, as compared to control artificial cerebrospinal fluid (aCSF) infusions (Fig. 5b and Supplementary Figs. 7i, 8a, and 9a). Similarly, the standard deviation in the MUA signal during periods of rest was decreased by $95 \pm 2\%$ of the control (Online Methods), indicating a nearly total silencing of spontaneous local spiking (Fig. 5g). The standard deviation of gamma-band power was reduced by $73 \pm 15\%$ (Fig. 5j). If resting hemodynamics arose primarily from local spiking, then the spontaneous fluctuations in CBV should show profound reductions in amplitude, essentially disappearing. However, all animals showed a significant and substantial remaining CBV fluctuations during periods of rest, despite the nearly complete elimination of local neural activity (resting CBV root-mean-squared amplitudes after muscimol infusions were $84 \pm 41\%$ of aCSF infusions, 95% confidence interval: [62–112%], bootstrap of the population mean, 2,000 resamples; Fig. 5c,d,g,j and Supplementary Fig. 8a). Muscimol infusions did not appreciably change the spatial patterns of the resting CBV fluctuations or the spectral power of the oscillations compared to the HRF prediction residuals (Supplementary Videos 2 and 3 and Supplementary Fig. 7d).

We also measured the diameters of arterioles after local infusion of aCSF or muscimol using two-photon microscopy^{7,39}. We measured from arterioles that would be well within the silenced region (mean vessel distance from infusion cannula: 0.75 ± 0.14 mm). These single-arteriole measures also showed small decreases in normalized fluctuation amplitudes at rest after muscimol infusions relative to aCSF infusions (resting root-mean-squared diameter fluctuations after muscimol infusions were $80 \pm 25\%$ of aCSF infusions, mixed-effects ANOVA, $P = 0.0015$, $t_{36} = 3.43$, $n = 19$ pial arterioles in 4 mice; $71 \pm 30\%$, $n = 8$ penetrating arterioles in 2 mice; $P = 0.36$, $t_{14} = 0.94$; Fig. 5d,e). These results indicate that at least half of the resting CBV fluctuations were not directly linked to local neural spiking.

Several studies have suggested that presynaptic activity alone, in the absence of postsynaptic spiking, is sufficient to drive the hemodynamic response^{2,40,41}. Hence, the remaining CBV oscillations could arise from glutamatergic release from distant cortico-cortical or subcortical projections, which would not be blocked by the local muscimol infusions. To determine whether presynaptic activity of long-range glutamatergic projections could account for the rest of the CBV oscillations through ionotropic receptors, we infused a cocktail of muscimol and ionotropic glutamate receptor antagonists, 6-cyano-7-nitroquinoxaline-2,3-dione (CNQX) and (2R)-amino-5-phosphonopentanoic acid (AP5), which inhibit AMPA and NMDA receptors, respectively ($n = 4$ mice; Online Methods). We again observed a strong reduction in the local multiunit activity ($96 \pm 2\%$; Fig. 5h), as well as a strong reduction in gamma-band power ($87 \pm 9\%$; Fig. 5k and Supplementary Figs. 8b and 9b). However, the reduction in CBV amplitude oscillations at rest ($40 \pm 20\%$; Fig. 5h,k) was not significantly lower than with the muscimol-only infusion, and did not account for the CBV or arteriole diameter oscillation ($12 \pm 47\%$ reduction, $n = 18$ vessels in 3 mice; Fig. 5f) that remained in the absence of local neural activity. These results indicate that, although presynaptic activity may contribute to some aspect of the spontaneous CBV fluctuations at rest, a large portion of the CBV fluctuations were not driven by either presynaptic neural activity or postsynaptic spiking.

Another possibility is that the remaining resting CBV fluctuations were driven by nonglutamatergic modulatory input^{12,42}, particularly noradrenergic input, as it has been shown in human studies⁴³ to play a role in resting state signals. To determine whether adrenergic input drove the remaining CBV oscillations after silencing local neural activity, we infused a cocktail of muscimol and adrenergic receptor blockers prazosin, yohimbine, and propranolol. The infusion of this cocktail again suppressed local spiking ($94 \pm 5\%$, $n = 5$; Fig. 5i and Supplementary Figs. 8c and 9c) and gamma-band power ($79 \pm 15\%$; Fig. 5l), and it reduced the amplitude of the CBV fluctuations by $40 \pm 17\%$, though not to a level significantly lower than the infusion of muscimol alone ($n = 5$, unpaired t test, one-sided, $P = 0.12$, $t_{12} = 1.24$). These data indicate that there was minimal contribution of adrenergic signaling to the generation of the ongoing CBV fluctuations in the absence of local spiking.

Because the cells in the vasculature are electrically coupled, there is a possibility that dilations in distant areas could propagate into the silenced region, which has been seen before in visual cortex⁴⁴. To determine whether propagation of vascular dilation could account for the observed CBV changes in the silenced region, we calculated the cross-correlation between CBV fluctuations within the ROI and the rest of the window from data taken after the infusion of muscimol and aCSF. If propagation of dilation accounts for the remaining CBV fluctuations, the correlation coefficient between these regions should increase and the time lag at which maximum correlation occurs should be delayed following muscimol infusion. We found that neither correlation nor lag times were significantly different between aCSF and muscimol trials ($n = 9$ mice, correlations: paired t test, $P = 0.12$, $t_5 = -1.9$; lags: paired t test, $P = 0.3$, $t_5 = -1.17$). This indicates that the remaining CBV fluctuations did not propagate

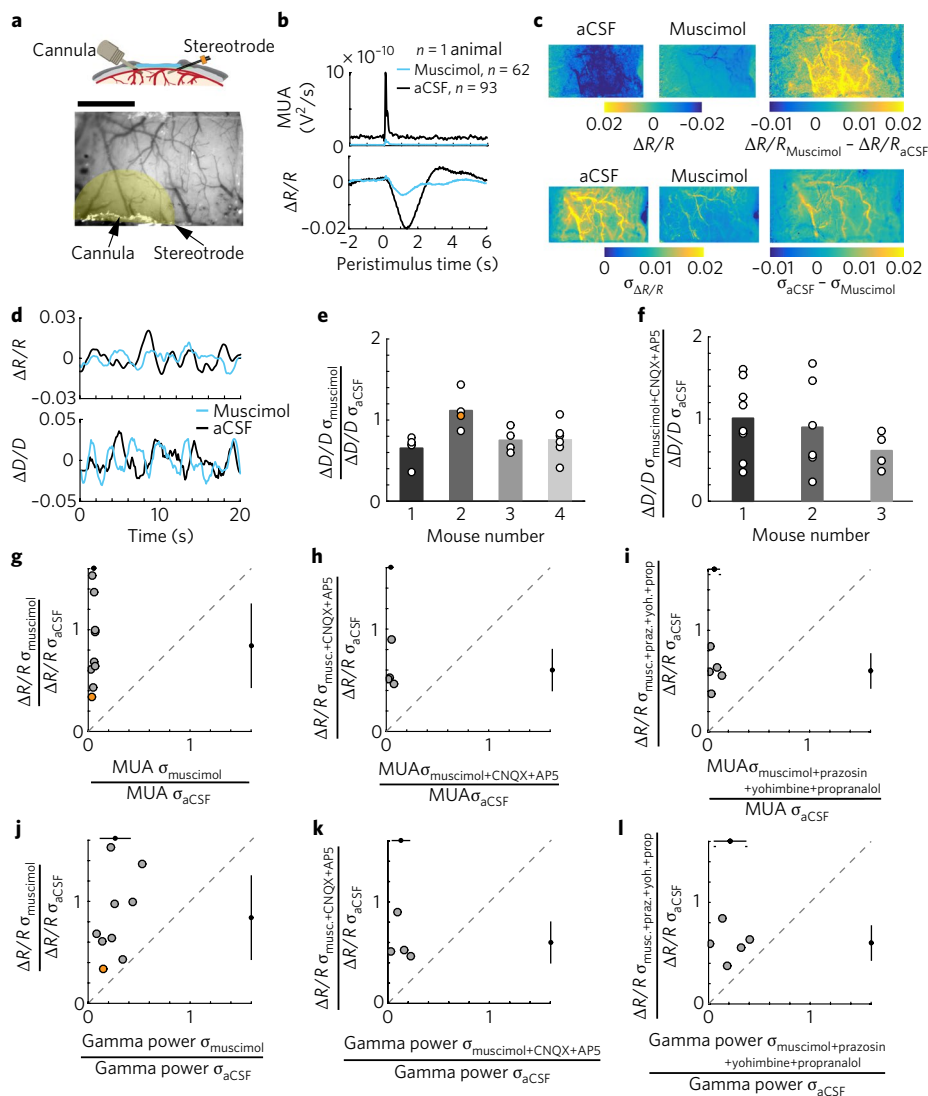


Fig. 5 | Spontaneous CBV fluctuations continue in the absence of neural activity and noradrenergic input. **a**, Top: schematic of the window-electrode-cannula preparation. Bottom: an image of a thinned skull window with cannula and electrode implants. The shaded yellow area indicates the ROI for CBV measurements. Scale bar, 1 mm. **b**, The average stimulation-evoked MUA following muscimol ($n = 62$ stimuli) and aCSF ($n = 93$ stimuli) infusion in a representative animal, showing reduced baseline and sensory-evoked MUA (top) and average stimulation-evoked increase in CBV (bottom) within the ROI in **a**. **c**, The average normalized pixel-wise CBV response to contralateral whisker stimulation (0.5–2 s after stimulation) across the thinned skull window for a single animal after aCSF infusion (top left, $n = 93$ stimuli) and after infusion of muscimol (top center, $n = 62$ stimuli). Top right shows the difference between aCSF infusion and muscimol infusion in the stimulation-triggered CBV response. The root-mean-squared deviation (σ) of resting CBV across the thinned skull window after aCSF infusion (bottom left) and after muscimol infusion is shown in the bottom center. The difference in the magnitude of the fluctuations under both conditions is shown in the bottom right. Example shows the same animal depicted in **a** and **b**. **d**, Example of resting CBV fluctuations following aCSF (black) and muscimol (blue) infusions in a single animal (top, same animal as in **a**). Bottom: normalized diameter measurements made from a single pial arteriole with two-photon laser scanning microscopy following aCSF (black) and muscimol (blue) infusions from a single animal during periods of rest. **e**, Population summary of the root-mean-square deviation in pial arteriole diameters (circles, $n = 19$) after muscimol infusion for 4 animals. Orange circle is the arteriole in lower plot in **d**. Bars indicate the mean for each animal. Vessel diameter oscillations were reduced following infusion of muscimol compared to aCSF (mixed-effects ANOVA, $P = 0.0015$, $t_{36} = 3.43$). **f**, As in **e** but for measurements taken after infusion of muscimol + CNQX + AP5 cocktail. We found no significant difference in the amplitudes of the normalized diameter fluctuations between muscimol + CNQX + AP5 and aCSF infusions (mixed-effects ANOVA, $n = 18$ vessels in 3 animals, $P = 0.22$, $t_{34} = 1.26$). **g**, Comparison of the root-mean-square deviation of resting MUA and CBV fluctuations. Black circles and error bars outside the axes show the population means and s.d. Orange circle is the mouse in **a–c**. The dashed gray line is unity. **h**, As in **g** but with a muscimol + CNQX + AP5 cocktail infusion. The resting CBV oscillation amplitude was not reduced compared to muscimol-only infusions ($n = 4$, unpaired t test, one sided, $P = 0.15$, $t_{11} = 1.11$). **i**, As in **g** but with an infusion of muscimol + prazosin + yohimbine + propranolol cocktail. The resting CBV oscillation was not significantly reduced as compared to muscimol-only infusions ($n = 5$, unpaired t test, one-sided, $P = 0.12$, $t_{12} = 1.24$). **j**, The root-mean-squared deviation of gamma-band neural power compared to CBV during periods of rest following muscimol infusion for all animals. Black circles and error bars outside the axes show the population means and s.d. **k**, As in **j** but for infusion of muscimol + CNQX + AP5 cocktail. The resting gamma-band power oscillations were reduced 87% compared to in controls but were not significantly different from reductions due to muscimol-only infusions (unpaired t test, one-sided, $P = 0.06$, $t_{11} = 1.73$). **l**, As in **j** but for an infusion of muscimol + prazosin + yohimbine + propranolol cocktail. The oscillations in gamma-band power were reduced 79% compared to in aCSF controls, which was not significantly different from results of muscimol-only infusions (unpaired t test, two sided, $P = 0.52$, $t_{12} = 0.66$).

from other regions within the window⁴⁴ (Supplementary Fig. 10). Taken together, these results indicate that resting CBV consists of contributions from local neural populations but that at least half of the resting CBV amplitude is not due to local neural processing, glutamatergic input, or adrenergic modulation. These remaining CBV oscillations peaked between 0.1 and 0.3 Hz, which is spectrally indistinguishable from neurally evoked CBV (Fig. 4a and Supplementary Fig. 7d), and were uncorrelated to sensory stimulation and movement (Fig. 4b–d).

Discussion

Comparison to previous measures of spontaneous and sensory-evoked neurovascular coupling

The correlations between neural activity and CBV we observed in the absence of sensory stimulation agreed well with those obtained in awake monkeys (mean \pm s.d.: $r=0.21 \pm 0.07$; Supplementary Fig. 4 versus Schölvinck et al.²⁰: $0.2 < r < 0.3$). We found a median $R^2=0.77$ for our gamma-band-power-derived prediction of stimulus-triggered average CBV, comparable to previous work in anesthetized primates (Logothetis et al.³¹ $R^2=0.76$ and $R^2=0.9$ reported for two different experimental sessions). Our trial-by-trial R^2 values for contralateral sensory stimulation were 0.34 and 0.30 for the gamma-band and MUA signals, respectively: very similar to those obtained by Goense et al.²² in awake primates. It seems unlikely that we are missing a signal detectable by conventional electrophysiological techniques.

Comparison of our sensory-evoked HRF prediction accuracy to other studies needs to take into account the strength and duration of the stimulus used, as well as whether this is for averaged stimulus-evoked hemodynamic changes or calculated on a trial-by-trial basis. The visual stimulations in these previous studies produced substantially larger and more prolonged spiking activity increases than our whisker stimulation (Logothetis et al.³¹: 10 s.d. above rest, stimulus 4–24 s duration; Goense et al.²²: 8–10 s.d. above rest, stimulus 15 s duration; Sirotnin & Das⁴: ~400% above resting rates, stimulus ~5 s duration; this study: 3 s.d. or 170% above rest, stimulus 10 ms duration). Notably, the R^2 between the actual and HRF-predicted CBV decreases as the stimulus intensity is reduced³². When we compare our results with stimuli that elicit comparable changes in neural activity with the awake primate data (low-contrast (~12.5%) visual stimulation in Cardoso et al.³²: ~200% increase; this paper: 170% increase), we are in good agreement (R^2 values: Cardoso et al.³²: 0.26, in their Supplementary Fig. 3; this paper: 0.31).

Recent work measuring cerebral blood volume and changes in the fluorescence of the genetically encoded calcium indicator GCaMP in awake head-fixed mice during periods without locomotion, but no other behavioral monitoring, reported good agreement between CBV and fluorescence changes⁴⁵. However, behaviors such as whisking, grooming (Fig. 3f), and brief (<1 s) movement events^{9,46} may contaminate these signals. Lastly, ‘ground truth’ experiments that simultaneously measure spiking activity with electrophysiology and fluorescence of calcium indicators show that even the best spike-detection algorithms detect far fewer than half the spikes and that this issue is worse at low firing rates, the regime under which resting-state activity is likely to be taking place²¹.

Implications of potential non-neuronal signals for hemodynamic imaging

Our results have several important implications for the interpretation of the neural correlates of hemodynamic signals. We showed that ‘spontaneous’ hemodynamic signals are driven by behaviors, such as active sensing and small body movements, that are typically ignored in human and animal imaging studies. These movements drive spatially localized hemodynamic signals and arterial dilations^{5,39}, and, because of the spatial specificity of these hemodynamic changes, a global regression procedure will be ineffective in removing these movement-evoked activations and may even

introduce artifacts⁴⁷. Our results particularly call into question previous studies that used spontaneous hemodynamic signals to assay neural differences that accompany disease, aging, and other conditions, as slight differences in behavior could drive differences in spontaneous dynamics independent of any underlying differences in neural activity.

We demonstrated that unlike the sensory-evoked response, in the true resting state at least 50% of the CBV signal is unrelated to local cortical processing, glutamatergic input, or noradrenergic modulation. While our results are consistent with the idea that these uncorrelated fluctuations in CBV have a non-neuronal origin, we cannot completely rule out other possible origins. For example, the spontaneous fluctuations could be driven by a subpopulation of vasodilatory neurons⁴⁸ or the recruitment of local astrocytes³⁴ whose activity we cannot detect in the MUA or LFP. However, to account for the additive CBV signal, any driver must have activity that is completely uncorrelated with other neurons and must have activity patterns that are unaffected by sensory stimulation or behavior. Additionally, for this alternative hypothesis to be true, when all of the vasodilatory input to the blood vessels is silenced during the local pharmacological infusions, the arterioles would need to have a homeostatic process that drives similar oscillations in diameter when the neural input is removed. To our knowledge, there are no such candidate neurons or processes in arteries. However, we hope that these results will motivate further investigations into the details of neurovascular coupling and smooth muscle biophysics³⁴. If these persistent CBV oscillations are of vascular origin, their function is not clear, though vascular pulsations have been implicated in driving fluid exchange in the lymphatic system⁴⁹.

Whatever the origin of the spontaneous CBV oscillations, our results clearly show that, in the absence of overt stimulation or behavior, hemodynamic signals are very poorly correlated with any conventional measure neural activity (Fig. 3). This poor correlation is in direct contrast to sensory-evoked and behaviorally evoked hemodynamic signals, which are relatively tightly coupled to the underlying neural activity. Subtracting off the global signal (Supplementary Fig. 7e) did not substantially improve this correlation, suggesting that there is no simple fix. Because of technical considerations, BOLD fMRI signals have even lower correlations with neural activity than the CBV signals we recorded here¹¹, making the problems observed here even more acute for human studies. This ‘noise’ will limit the ability to detect and accurately infer ongoing neural activity and can only be surmounted by massive averaging. However, we note that these results do not refute the existence of functional connectivity, which has been validated using direct assays of neural activity⁵⁰.

In light of these results, we propose fundamental changes in the way resting-state studies should be performed and interpreted. First, it is essential to measure behavior in a very detailed way during imaging to ensure that behavioral variability does not drive differences in spontaneous activity between groups or across conditions. Small differences in the frequency of active-sensing behaviors and movements will drive large differences in spontaneous hemodynamic signals. Second, during periods of true rest, hemodynamic signals should not be interpreted as being solely driven by electrical activity in neurons. Rather, these signals have contributions from other processes that are additive to, and uncorrelated with, neurally evoked CBV changes.

Note added in proof: A recent paper⁷⁴ also found correlations between gamma band power and spontaneous hemodynamic signals in awake mice.

Methods

Methods, including statements of data availability and any associated accession codes and references, are available at <https://doi.org/10.1038/s41593-017-0007-y>.

Received: 6 April 2017; Accepted: 20 September 2017;
Published online: 6 November 2017

References

1. Fox, M. D. & Raichle, M. E. Spontaneous fluctuations in brain activity observed with functional magnetic resonance imaging. *Nat. Rev. Neurosci.* **8**, 700–711 (2007).
2. Smith, S. M. et al. Functional connectomics from resting-state fMRI. *Trends Cogn. Sci.* **17**, 666–682 (2013).
3. Maier, A. et al. Divergence of fMRI and neural signals in V1 during perceptual suppression in the awake monkey. *Nat. Neurosci.* **11**, 1193–1200 (2008).
4. Sirotnin, Y. B. & Das, A. Anticipatory haemodynamic signals in sensory cortex not predicted by local neuronal activity. *Nature* **457**, 475–479 (2009).
5. Huo, B.-X., Smith, J. B. & Drew, P. J. Neurovascular coupling and decoupling in the cortex during voluntary locomotion. *J. Neurosci.* **34**, 10975–10981 (2014).
6. Vazquez, A. L., Fukuda, M., Crowley, J. C. & Kim, S.-G. Neural and hemodynamic responses elicited by forelimb- and photo-stimulation in channelrhodopsin-2 mice: insights into the hemodynamic point spread function. *Cereb. Cortex* **24**, 2908–2919 (2014).
7. Drew, P. J., Shih, A. Y. & Kleinfeld, D. Fluctuating and sensory-induced vasodynamics in rodent cortex extend arteriole capacity. *Proc. Natl. Acad. Sci. USA* **108**, 8473–8478 (2011).
8. Gao, Y. R. et al. Time to wake up: Studying neurovascular coupling and brain-wide circuit function in the un-anesthetized animal. *Neuroimage* **153**, 382–398 (2017).
9. Huo, B.-X., Gao, Y.-R. & Drew, P. J. Quantitative separation of arterial and venous cerebral blood volume increases during voluntary locomotion. *Neuroimage* **105**, 369–379 (2015).
10. Hall, C. N. et al. Capillary pericytes regulate cerebral blood flow in health and disease. *Nature* **508**, 55–60 (2014).
11. Kim, S.-G. & Ogawa, S. Biophysical and physiological origins of blood oxygenation level-dependent fMRI signals. *J. Cereb. Blood Flow Metab.* **32**, 1188–1206 (2012).
12. Logothetis, N. K. What we can do and what we cannot do with fMRI. *Nature* **453**, 869–878 (2008).
13. Hirano, Y., Stefanovic, B. & Silva, A. C. Spatiotemporal evolution of the functional magnetic resonance imaging response to ultrashort stimuli. *J. Neurosci.* **31**, 1440–1447 (2011).
14. Fukuda, M. et al. Localization of activity-dependent changes in blood volume to submillimeter-scale functional domains in cat visual cortex. *Cereb. Cortex* **15**, 823–833 (2005).
15. Guipponi, O., Odoard, S., Pinède, S., Wardak, C. & Ben Hamed, S. fMRI Cortical correlates of spontaneous eye blinks in the nonhuman primate. *Cereb. Cortex* **25**, 2333–2345 (2015).
16. Galton, F. The measure of fidget. *Nature* **32**, 174–175 (1885).
17. O'Connor, D. H. et al. Neural coding during active somatosensation revealed using illusory touch. *Nat. Neurosci.* **16**, 958–965 (2013).
18. Liu, X. & Duyn, J. H. Time-varying functional network information extracted from brief instances of spontaneous brain activity. *Proc. Natl. Acad. Sci. USA* **110**, 4392–4397 (2013).
19. Laumann, T. O. et al. On the stability of BOLD fMRI correlations. *Cereb. Cortex* **27**, 4719–4732 (2017).
20. Schölvinck, M. L., Maier, A., Ye, F. Q., Duyn, J. H. & Leopold, D. A. Neural basis of global resting-state fMRI activity. *Proc. Natl. Acad. Sci. USA* **107**, 10238–10243 (2010).
21. Theis, L. et al. Benchmarking spike rate inference in population calcium imaging. *Neuron* **90**, 471–482 (2016).
22. Goense, J. B. M. & Logothetis, N. K. Neurophysiology of the BOLD fMRI signal in awake monkeys. *Curr. Biol.* **18**, 631–640 (2008).
23. de Kock, C. P. J. & Sakmann, B. Spiking in primary somatosensory cortex during natural whisking in awake head-restrained rats is cell-type specific. *Proc. Natl. Acad. Sci. USA* **106**, 16446–16450 (2009).
24. Chapin, J. K. & Lin, C. S. Mapping the body representation in the SI cortex of anesthetized and awake rats. *J. Comp. Neurol.* **229**, 199–213 (1984).
25. Sachidhanandam, S., Sreenivasan, V., Kyriakatos, A., Kremer, Y. & Petersen, C. C. H. Membrane potential correlates of sensory perception in mouse barrel cortex. *Nat. Neurosci.* **16**, 1671–1677 (2013).
26. Boynton, G. M., Engel, S. A., Glover, G. H. & Heeger, D. J. Linear systems analysis of functional magnetic resonance imaging in human V1. *J. Neurosci.* **16**, 4207–4221 (1996).
27. Kay, K. N., Naselaris, T., Prenger, R. J. & Gallant, J. L. Identifying natural images from human brain activity. *Nature* **452**, 352–355 (2008).
28. O'Connor, D. H. et al. Vibrissa-based object localization in head-fixed mice. *J. Neurosci.* **30**, 1947–1967 (2010).
29. Sreenivasan, V. et al. Movement initiation signals in mouse whisker motor cortex. *Neuron* **92**, 1368–1382 (2016).
30. Howarth, C., Gleeson, P. & Attwell, D. Updated energy budgets for neural computation in the neocortex and cerebellum. *J. Cereb. Blood Flow Metab.* **32**, 1222–1232 (2012).
31. Logothetis, N. K., Pauls, J., Augath, M., Trinath, T. & Oeltermann, A. Neurophysiological investigation of the basis of the fMRI signal. *Nature* **412**, 150–157 (2001).
32. Cardoso, M. M. B., Sirotnin, Y. B., Lima, B., Glushenkova, E. & Das, A. The neuroimaging signal is a linear sum of neurally distinct stimulus- and task-related components. *Nat. Neurosci.* **15**, 1298–1306 (2012).
33. Murphy, K., Birn, R. M. & Bandettini, P. A. Resting-state fMRI confounds and cleanup. *Neuroimage* **80**, 349–359 (2013).
34. Attwell, D. et al. Glial and neuronal control of brain blood flow. *Nature* **468**, 232–243 (2010).
35. Mayhew, J. E. W. et al. Cerebral vasomotion: a 0.1-Hz oscillation in reflected light imaging of neural activity. *Neuroimage* **4**, 183–193 (1996).
36. Thrane, A. S. et al. General anesthesia selectively disrupts astrocyte calcium signaling in the awake mouse cortex. *Proc. Natl. Acad. Sci. USA* **109**, 18974–18979 (2012).
37. Osol, G. & Halpern, W. Spontaneous vasomotion in pressurized cerebral arteries from genetically hypertensive rats. *Am. J. Physiol.* **254**, H28–H33 (1988).
38. Wölfe, S. E. et al. Non-linear relationship between hyperpolarisation and relaxation enables long distance propagation of vasodilatation. *J. Physiol. (Lond.)* **589**, 2607–2623 (2011).
39. Gao, Y. R., Greene, S. E. & Drew, P. J. Mechanical restriction of intracortical vessel dilation by brain tissue sculpts the hemodynamic response. *Neuroimage* **115**, 162–176 (2015).
40. Mishra, A. et al. Astrocytes mediate neurovascular signaling to capillary pericytes but not to arterioles. *Nat. Neurosci.* **19**, 1619–1627 (2016).
41. Chaigneau, E. et al. The relationship between blood flow and neuronal activity in the rodent olfactory bulb. *J. Neurosci.* **27**, 6452–6460 (2007).
42. Drew, P. J., Duyn, J. H., Golanov, E. & Kleinfeld, D. Finding coherence in spontaneous oscillations. *Nat. Neurosci.* **11**, 991–993 (2008).
43. van den Brink, R. L. et al. Catecholaminergic neuromodulation shapes intrinsic MRI functional connectivity in the human brain. *J. Neurosci.* **36**, 7865–7876 (2016).
44. O'Herron, P. et al. Neural correlates of single-vessel haemodynamic responses in vivo. *Nature* **534**, 378–382 (2016).
45. Ma, Y. et al. Resting-state hemodynamics are spatiotemporally coupled to synchronized and symmetric neural activity in excitatory neurons. *Proc. Natl. Acad. Sci. USA* **113**, E8463–E8471 (2016).
46. Nimmerjahn, A., Mukamel, E. A. & Schnitzler, M. J. Motor behavior activates Bergmann glial networks. *Neuron* **62**, 400–412 (2009).
47. Murphy, K., Birn, R. M., Handwerker, D. A., Jones, T. B. & Bandettini, P. A. The impact of global signal regression on resting state correlations: are anti-correlated networks introduced? *Neuroimage* **44**, 893–905 (2009).
48. Cauli, B. et al. Cortical GABA interneurons in neurovascular coupling: relays for subcortical vasoactive pathways. *J. Neurosci.* **24**, 8940–8949 (2004).
49. Iltif, J. J. et al. Cerebral arterial pulsation drives paravascular CSF-interstitial fluid exchange in the murine brain. *J. Neurosci.* **33**, 18190–18199 (2013).
50. Mohajerani, M. H. et al. Spontaneous cortical activity alternates between motifs defined by regional axonal projections. *Nat. Neurosci.* **16**, 1426–1435 (2013).

Acknowledgements

We thank L. Abbott, M. Adams, P. Blinder, D. Feldman, and N. Zhang for comments on the manuscript, and J. Berwick, D. Kleinfeld, and C. Mateo for discussions. This work was supported a Scholar Award from the McKnight Endowment Fund for Neuroscience, and grants R01NS078168, R01EB021703, and R01NS079737 from the NIH to P.J.D.

Author contributions

A.T.W. and P.J.D. designed the experiments, A.T.W., C.E., and Q.Z. performed experiments and analyzed the data, A.T.W. and P.J.D. wrote the paper.

Competing financial interests

The authors declare no competing financial interests.

Additional information

Supplementary information is available for this paper at <https://doi.org/10.1038/s41593-017-0007-y>.

Reprints and permissions information is available at www.nature.com/reprints.

Correspondence and requests for materials should be addressed to P.J.D.

Publisher's note: Springer Nature remains neutral with regard to jurisdictional claims in published maps and institutional affiliations.

Methods

Animals and procedures. All procedures outlined below were conducted in accordance with guidelines from the Institutional Animal Care and Use Committee (IACUC) of Penn State. Data were acquired from 42 male C57-BJ6 mice (Jackson Laboratory) between 3 and 8 months of age (12 for HRF and behavior measurements, 3 for window-only controls, 3 for transected motor nerve controls, 7 for two-photon laser scanning microscopy (2PLSM), and 17 for cannula implantation and infusion experiments). Mice were given food and water ad libitum and maintained on 12-h light/dark cycles in isolated cages during the period of experiments. All imaging took place during the light cycle period. Sample sizes were chosen to be consistent with previous studies^{6–9}. Data collection and analysis were not performed blind to the conditions of the experiments. Drug infusions were counterbalanced across animals. See the Life Sciences Reporting Summary for more details.

Surgery. Electrode, cannula, and window implantation procedure for intrinsic optical signal (IOS) imaging experiments. Mice were anesthetized with 2% isoflurane (in oxygen) for all surgical procedures. A custom-machined titanium metal bar, used to fix the mice in place during imaging, was attached to the skull with cyanoacrylate glue (Vibra-Tite, 32402). The bar was positioned along the midline and just posterior to the lambda cranial suture. A reinforced thinned-skull window was created over the left hemisphere as described previously^{5,51}. A 4–10-mm² area of skull was thinned over the whisker representation of somatosensory cortex (Fig. 1c,d). A Teflon-coated tungsten-wire (AM systems, #795500) stereotrode was inserted into the barrel cortex at 30–45° from the horizontal along the rostrocaudal axis using a micromanipulator (Sutter Instruments, MP285) through a small hole made at the edge of the thinned area, so that the electrode tips were within the window (Fig. 1c). The hole was sealed with cyanoacrylate glue. In a subset of mice ($n=17$), a small craniotomy was made at the edge of the thinned area of skull, and a cannula (Plastics One, C315DCS, C315GS-4) was inserted into the upper layers of cortex (Fig. 5a and Supplementary Figs. 1g and 8). The cannula was attached to the skull with cyanoacrylate glue and dental acrylic. The thinned area of skull was reinforced with a fitted #1 glass coverslip (Electrode Microscopy Sciences, #72200). Three self-tapping, 3/32-inch #000 (J.I. Morris) screws were inserted into the contralateral parietal and frontal bone and ipsilateral frontal bone. A stainless-steel wire (A-M Systems, #792800) was wrapped around the screw implanted in the frontal bone contralateral to the window and used as an electrical ground for neural recordings. The titanium bar, screws, and tungsten wires were secured with black dental acrylic resin (Lang Dental MFG. Co., REF 1530) to minimize light reflection. The animals were allowed to recover for 2–3 d before habituation. Neither electrode nor cannula implantation affected the hemodynamic response (Supplementary Fig. 1f).

Cannula and window implantation for two-photon laser scanning microscopy (2PLSM). As above, mice were anesthetized with isoflurane for all surgical procedures. A titanium head bar was placed as described above, and a 4–6-mm² polished and reinforced thinned-skull window was created over the forepaw/hindpaw representation of somatosensory cortex of the left hemisphere⁵¹. After polishing the skull with 3F grit (Covington Engineering, Step Three 3F-400), a small craniotomy was made to insert the cannula into the upper layers of cortex near the forepaw/hindpaw representation of cortex. The thinned area of the skull was reinforced with a fitted #0 glass coverslip (Electrode Microscopy Sciences, #72198). Two self-tapping screws were inserted into the contralateral parietal and ipsilateral frontal bone. The titanium bar, cannula, and screws were secured with black dental acrylic resin. The animals were allowed to recover for 2–3 d before habituation.

Facial nerve transections. Animals were anesthetized with 2% isoflurane and bilateral incisions were made posterior to the whisker pad. The facial nerve was transected with iris scissors²⁵, and the incisions were sutured. Topical antibiotic ointment was applied (Neosporin), and animals were allowed to recover for 2–3 d before habituation to head fixation. Animals were monitored to verify that no vibrissa movement occurred following transection.

Histology. At the end of the experiment, animals were deeply anesthetized with 5% isoflurane. The mice were transcardially perfused with heparinized saline and then fixed with 4% paraformaldehyde. Fiduciary marks were made in each of the corners of the cranial window. The brains were extracted and sunk in a 30% sucrose/4% paraformaldehyde solution. The flattened cortices were sectioned tangentially (60 µm per section) using a freezing microtome and stained for the presence of cytochrome oxidase (CO). Whisker barrels were visible in layer IV of CO-stained sections, allowing the alignment of the windows and stereotrodes with respect to the barrel cortex^{52,53}. The laminar locations of the stereotrodes were categorized as supragranular, granular, or infragranular by identifying the first cortical section without visible electrode tracks relative to sections showing whisker barrels.

Physiological measurements. Data from intrinsic optical signal and electrophysiology experiments were acquired with a custom-written LabVIEW

program (ATW and PJD, version 11.0, 64-bit Windows 7, National Instruments, Austin, TX). Data from 2PLSM experiments was acquired using Sutter MCS software (Sutter Instruments, Novato, CA). All experiments were performed with mice in sound-attenuating boxes.

Habituation. Animals were gradually acclimated to head-fixation and stimulation over three habituation sessions. Mice that received whisker stimulation ($n=31$) were acclimated to head-fixation for 15–30 min during the first session. In subsequent sessions, they began to receive air puffs directed at the whiskers and were head-fixed for longer durations (>60 minutes). Mice that were imaged using 2PLSM ($n=7$) were acclimated to the spherical treadmill (60 mm radius) over 3 d. During the first session, they were head-fixed for 15 min. On subsequent days, the time was increased to ~60 min. Mice were monitored for any signs of distress during habituation. In all cases, the mice exhibited normal behaviors such as exploratory whisking and occasional grooming after being head-fixed. Heart-rate-related fluctuations were detectable in the intrinsic optical signal (see below) and remained between 7 and 14 Hz for all mice during and after habituation. This is near the mean heart-rate (~12 Hz) telemetrically recorded from mice in their home cage⁵⁴. Experimental data were taken over 2–5 imaging sessions.

Intrinsic optical signal (IOS) imaging. Twenty minutes before the experiments, the mice were briefly (<1 min) anesthetized with isoflurane (5%) and fixed into the imaging apparatus using the attached titanium head bar. When fixed, the animal's body was supported in a clear plastic tube ($n=31$) or on a ball ($n=4$). The imaging apparatus and head-fixing apparatus were arranged to avoid incidental whisker contact during whisking. Blood volume was measured by illuminating the cranial window with three collimated and filtered 530 ± 5-nm LEDs (Thor Labs, FB530-10, M530L2). This wavelength is an isosbestic point of the hemoglobin light absorption curves. Reflected light intensity from the surface of the brain at this wavelength gives a measurement of the total hemoglobin concentration, which we used as a measure of CBV. Decreased reflectance from the cranial window corresponds to increased absorption by hemoglobin due to increased CBV. The cranial window was imaged with a Dalsa 1M60 Pantera CCD camera (Phase One, Cambridge MA) positioned directly above the mouse. Light entering the camera was filtered using a mounted green filter (Edmund Optics, Barrington NJ, #46540) to block the light used for whisker tracking. Images (256 × 256 pixels, 15 µm per pixel, 12-bit resolution) were acquired at 30 Hz^{25,55}. The data were then low-pass filtered (3 Hz, Butterworth, order = 4, Matlab function: butter, filtfilt) to remove heart-rate-related fluctuations.

Electrophysiology. Neural activity was recorded simultaneously with the IOS as differential potentials between the two leads of Teflon-insulated tungsten microwires (A-M Systems, #795500)⁵. Stereotrode microwires with an interelectrode spacing of ~100 µm were threaded through polyimide tubing (A-M Systems, #822200). Electrode impedances were between 70 and 120 kΩ at 1 kHz. The acquired signals were amplified (World Precision Instruments, DAM80), bandpass filtered between 0.1 and 10 kHz (Brownlee Precision, Model 440) during acquisition, then digitized at 20 kHz (National Instruments, Austin TX, PCI-6259). We were able to detect individual spikes in all animals (Supplementary Fig. 1c), but spiking responses to whisker stimulation and volitional whisking varied among animals²³. We quantified spiking activity using the multiunit average (MUA), which is the power of the signal within the 300–3,000 Hz band²². Power was calculated by digitally bandpass filtering the raw neural signal (Matlab function: butter, filtfilt; filter order = 4). The result was squared, low-pass filtered below 10 Hz, and resampled at 30 Hz. A baseline power (P_0) was computed by averaging the band-limited power during periods of the imaging session in which no stimulation or volitional movement occurred. The normalized power was then calculated as $\Delta P/P_0 = [P - P_0]/P_0$. Gamma-band power was calculated in the same manner using the 40–100 Hz band of the LFP. Neither the LFP nor the MUA signals showed significant changes in sensory evoked amplitude (gamma-band power: $P = 0.94$, $t_{61} = 0.08$; MUA: $P = 0.19$, $t_{61} = 1.33$) or neural variance (gamma-band power: $P = 0.81$, $t_{61} = 2.45$; MUA: $P = 0.28$, $t_{61} = 1.09$) from day to day ($n=63$, iteratively reweighted least squares, bisquare weighting, Matlab function: robustfit), indicating that the recordings were stable across imaging sessions. The spatial resolution of the LFP depends on the distance between the recording electrodes. Differential recordings sample the volume of tissue spanned by the electrodes, and if these electrodes are closely spaced^{56,57}, they provide a very localized (equivalent to the electrode spacing) measure of the LFP. Using a remote reference can contaminate the LFP signal if activity in the remote area is nonstationary, as is the case in an awake animal. Signals from spiking activity are much more localized, and our electrode recorded neural activity from a sphere of ~100 µm in diameter⁵⁸. For infusion experiments, band-limited neural power was normalized to the mean amplitude during periods of rest from the same session prior to infusion.

Two-photon microscopy. Mice ($n=7$) were briefly anesthetized with isoflurane and retro-orbitally injected with 50 µL 5% (weight/volume) fluorescein-conjugated dextran (70 kDa; Sigma-Aldrich)^{59,60}, and then fixed on a spherical treadmill (see “Behavior tracking” section below). Imaging was done on a Sutter Movable Objective Microscope with a 20×, 0.9 NA objective (Olympus). A MaiTai

HP (Spectra-Physics, Santa Clara, CA) laser tuned to 800 nm was used for fluorophore excitation. Individual arteries ($n = 19$ pial, 5 vessels/mouse; $n = 8$ penetrating, 2–3 vessels/mouse) were imaged at nominal frame rate of 8 Hz for 5 min using 10–15 mW of power exiting the objective. The same arteriole segments in the limb representation of somatosensory cortex were imaged after aCSF and muscimol infusions.

Vibrissa stimulation. Animals were awake and engaged in whisking behavior during IOS data acquisition. Brief (0.1-s duration) puffs of air were delivered to the ipsilateral and contralateral whiskers through a thin plastic tube (length 130 mm, diameter 2 mm). Air puffs were directed to the distal ends of the whiskers at an angle parallel to the face to prevent stimulation of other parts of the head or face. An additional air puffer was set up to point away from the body for use as an auditory stimulus. The puffs were delivered via solenoid actuator valves (Sizto Tech Corporation, 2V025 1/4) at constant air pressure (10 psi) maintained by an upstream regulator (Wilkerson, R03-02-000). Air puffs were separated by intervals of 10–60 s, and the order of all sensory stimulation was randomized, with a nominal ratio of three contralateral stimuli for every ipsilateral or auditory stimulation. Auditory and ipsilateral stimuli were omitted from the principal analysis because their responses were primarily related to stimulus-provoked movement (Supplementary Fig. 1h).

Behavioral measurement. For IOS imaging experiments, the whiskers contralateral to the imaged hemisphere were diffusely illuminated from below with 625-nm light (Edmund Optics, #66-833) and imaged using a Basler A602f camera (Edmund Optics, Barrington NJ) at 150 frames per s. The imaging region was restricted to the area just adjacent to the face, with the long axis of the image parallel to the line of the face where whisker curvature is minimal and the full range of whisker movement could be captured. As additional behavioral measurements, the animal was monitored using a webcam (Microsoft LifeCam Cinema), and a force sensor (Tekscan, Flexiforce A201, Boston MA) was placed below the clear plastic tube to detect body movement. A threshold was established by examining force measurements when each animal was clearly moving during the trial. Changes in force that exceeded the threshold were flagged as body movements by the animal.

For 2PLSM imaging ($n = 7$) and for a subset of IOS experiments ($n = 4$), mice were fixed using the attached head bar on a spherical treadmill with one degree of freedom⁵⁶⁰. The treadmill was coated with antislip tape and attached to an optical rotary encoder (US Digital, E7PD-720-118) to monitor rotational velocity. For mice on the treadmill, ball movements were used to detect animal behavior in lieu of whisker tracking in order to identify periods of rest.

Intracortical infusions. For IOS imaging, animals were placed in the imaging apparatus as described above. We then acquired 10 min of CBV, neural, and behavioral data with the dummy cannula in place. The dummy cannula was then slowly removed and replaced with an infusion cannula (Plastics One, C315IS-4). The interface between the infusion cannula and the guide cannula was sealed with Kwik-Cast (World Precision Instruments). Muscimol (10 mM)⁶¹ alone, and a muscimol (10 mM) + CNQX (600 μ M) + AP5 (2.5 mM) cocktail, a muscimol (10 mM) + prazosin (1 mM) + yohimbine (1 mM) + propranolol (1 mM) cocktail⁶², or aCSF alone were infused at a rate of 25 nL/min for a total volume of 500 nL. CBV and neural activity were constantly monitored during the infusion to ensure that cannula placement did not affect neural activity or hemodynamic signals. Autoradiography⁶³, immunohistochemistry⁶⁴, and gene expression⁶⁵ studies have failed to detect GABA-A receptors in the small vessels of the cerebral vasculature whose dilations we measured here. Blocking GABA-A mediated transmission does not block optogenetically evoked vasodilation by interneurons⁶⁶, indicating that GABA-A receptors do not mediate activity-evoked vasodilation. To validate that the cannula was patent, infusions were combined with 1% fluorescein isothiocyanate (FITC). To verify successful infusion, FITC fluorescence was visualized by capturing images of the thinned skull window while it was illuminated with blue light (470 nm, Thor Labs, M470L2) every ~5 min. Pharmacological treatments and aCSF were each infused in a counterbalanced order. All mice received both infusions of drugs and an aCSF control, so no randomization was needed. Neural and CBV measurements were acquired during the infusion as an additional means of assaying the efficacy of pharmacological manipulation. Pharmacological data were only used if the MUA amplitude was confirmed to have decreased by >80% compared to aCSF. Baseline reflectance from the ROI increased as neural activity was increased, indicating decreased CBV. CBV baselines prior to this decrease were used for normalization. Some animals exhibited occasional bursts of neural activity accompanied by large CBV changes (10–15% peak to peak) approximately 1 h after muscimol infusions. Data taken after a burst of activity were omitted from subsequent analyses. For 2PLSM imaging, mice were head-fixed on the spherical treadmill. Infusion cannulas were placed and infusions were conducted as described for IOS imaging, except that FITC was not infused. Animals were kept in place for 20 min after the infusion and then moved to the imaging apparatus. The infusion cannulas were kept in place for the duration of the imaging session. Baseline diameter constrictions were observed during infusion, in accordance with intrinsic data. Vessel measurements occurred >45 min after the start of infusion.

Data analysis. All analyses were conducted using custom-written code (by A.T.W., C.E., Q.Z., and P.J.D.) in Matlab 2015a (MathWorks).

Alignment of anatomical areas to CBV imaging data. The location of the thinned-skull window with respect to anatomical landmarks of the cortex was obtained by aligning the surface vasculature in the most superficial histological sections with the vasculature visible through the window during imaging. Deeper sections were aligned using fiducial marks and penetrating vessels as landmarks. All image alignment was performed using affine transformations in Adobe Illustrator CS6 (Adobe Systems).

Detection and quantification of whisker motion. Images of whiskers during data acquisition were converted into a relative whisker position by applying the Radon transform (Matlab function: `radon`) to each image. Peaks from the resulting sinogram correspond to a position and angle of whiskers in the image. The mean whisker angle was extracted by identifying the angle of the sinogram that had the largest variance in the position dimension⁵⁹. The mean whisker position was digitally low-pass filtered (<30 Hz) using a fourth-order Butterworth filter (Matlab functions: `butter`, `filtfilt`). Whisker acceleration was obtained from the second derivative of the filtered position and binarized according to the equation

$$\delta(t) = H(|a_t| - a_c) = \begin{cases} 1, & |a_t| \geq a_c \\ 0, & |a_t| < a_c \end{cases}$$

where a_t is the acceleration at time t , and a_c is the acceleration threshold. Whisker acceleration was used since it is directly related to the force on the whisker. The whisking thresholds were empirically defined for each animal by identifying whisker accelerations that occurred when the animal was clearly whisking. Similarly, periods of rest were identified during which the animal was not making exploratory whisker movements, to establish acceleration values during nonwhisking periods. Any isolated acceleration values that fell between these thresholds were omitted from analysis. Ambiguous acceleration values that occurred within 0.5 s of a clear whisk were considered part of the bout of whisking.

2PLSM image processing. Individual frames from 2PLSM imaging were aligned using a rigid registration algorithm to remove motion artifacts in the x - y plane³⁹. Visual inspection of movies indicated that there was minimal z -axis motion. A rectangular box was manually drawn around a short segment of the vessel and the pixel intensity was averaged along the long axis⁷. Pixel intensity was used to calculate diameter from the full-width at half-maximum. Diameters of penetrating arterioles were calculated using the thresholded in Radon space (TiRS) algorithm^{59,67}. Periods of rest were segregated using locomotion events measured with the rotary encoder⁹. For each 5-min trial, diameter measurements were normalized to the average diameter during periods of rest. The diameters were smoothed with a third-order, 15-point Savitzky–Golay filter (Matlab function: `sgolayfilt`). During all resting periods, the spontaneous fluctuations were compared by calculating the normalized standard deviation from the average baseline diameter. The standard deviation of the fractional diameter changes after pharmacological infusion were normalized by the standard deviations after fractional diameter changes after aCSF infusion for the same vessel segment.

Heart rate detection. We tracked heart rates by calculating time–frequency spectrograms with a 2-s sliding window on the median window reflectance (Supplementary Fig. 2a; Chronux Toolbox version 2.11 function: `mtspecgram`; <http://chronux.org/>)^{55,68}. We took the derivative of the median window reflectance to reduce the $1/f$ trend in the spectrum before calculating the time–frequency spectrogram and to improve detection of peaks in spectral power. The heart rate was identified as the frequency with the maximum spectral power in the 5–15 Hz band.

Behavioral state categorization. For analysis of HRF dynamics, data were separated into three behavioral categories: contralateral whisker stimulation, volitional whisking, and rest. The period (6 s) following an air puff to the contralateral whiskers was isolated, provided that the animal was quiescent at the time of stimulation. Volitional whisking behaviors were defined as the period following a voluntary movement of the whiskers with at least 3 s of rest prior to the whisker movement. The duration of the movement was also tracked and separated into short (<2 s) and long (>2 s) movements. Resting behavior was defined as the absence of stimulation or movement. Periods of rest lasting <10 s were considered to be transitions between behaviors and omitted from the principal analysis. Data corresponding to whisker stimulation and volitional whisking were isolated beginning 4 s before and 6 s after behavior onset.

For two-photon microscopy data ($n = 7$) and a subset of IOS animals ($n = 4$), behavior was categorized by monitoring movement on a spherical treadmill with one degree of freedom^{5,46}. Movement events were detected by applying a fifth-order low-pass filter (10 Hz, Butterworth, Matlab function: `butter`, `filtfilt`) to the velocity signal as measured by the velocity encoder, taking the derivative of the velocity, and then comparing the absolute value of the resulting acceleration to a threshold of

10 cm/s²,^{39,60}. Periods of rest were categorized based on the binarized detection of the treadmill acceleration:

$$\delta(t) = H(|a_t| - a_b) = \begin{cases} 1, & |a_t| \geq a_b \\ 0, & |a_t| < a_b \end{cases}$$

where a_t is the acceleration at time t , and a_b is the treadmill acceleration threshold. Resting periods were those starting 2 s (2PLSM) and 4 s (IOS) after the end of any running event and lasting more than 10 s with no detected movement.

Region of interest selection and baseline. An ROI for each mouse was created by identifying image pixels within the barrel cortex that were correlated with neural activity when the animal was at rest. To identify correlated pixels, images of the thinned skull window and MUA data during periods of rest were chosen and normalized to the resting mean (Fig. 1d). The mean reflectance from the entire window at each timepoint (the global signal) was then subtracted from each pixel. The cross-correlation was calculated (Matlab function: `xcorr`) between the reflectance signal of each mean-subtracted pixel and the MUA and normalized by the autocorrelations. The median correlation coefficients between lagged MUA (0.5–1.5 s; Fig. 1d) and the intensity of each pixel were plotted (Fig. 1d). This spatial correlation map was overlaid on a histological reconstruction of the window and electrode locations (Fig. 1d). In all animals, pixels with correlations between lagged MUA (0.5–1.5 s; Fig. 1d) and CBV greater than $r = 0.1$ were adjacent to the stereotrode site and localized near the whisker barrels. A circular region of interest (ROI) was created to encompass pixels that were near the stereotrode, that were within the barrel cortex, and that showed positive correlations between the CBV signal and MUA at a 0.5–1.5-s lag ($r > 0.1$; ROI area: 0.6 ± 0.1 mm²). For mice with an implanted cannula, regions of interest within the thinned-skull window were created by histologically identifying the location of the cannulas and stereotrodes and drawing a semicircular region, with the cannula at the center and radius equal to the distance from the cannula to the electrode (Fig. 5a and Supplementary Fig. 8). Calculations of the reflectance baselines and normalization procedures were as described above. The ROIs of three animals spanned the window and were omitted from the analysis comparing the CBV within the ROI to the rest of the window.

Periods of rest were identified for each imaging session, and the mean intensity within the ROI was averaged over the duration of the resting data, giving a single reflectance baseline (R_b) for each animal and imaging session. The ROI reflectance was used as the measure of CBV for all experiments. The fractional change in ROI reflectance was given by $\Delta R/R_b = [R - R_b]/R_b$. For infusion experiments, only resting periods prior to infusion were used for normalization.

Triggered spectrograms. Time–frequency spectrograms were calculated for the duration of the trial using multitapered spectral analysis (Matlab Chronux toolbox version 2.11 function: `mtspectrum`, <http://chronux.org/>)⁶⁸. The time bins surrounding stimulation and whisking events were isolated, and each frequency band was normalized to the resting baseline and then averaged over behavioral events.

Cross-correlation calculations. Neural signals were separated into frequency bands (~10-Hz resolution) within the LFP band by calculating the spectrogram (Matlab Chronux toolbox version 2.11 function: `mtspectrum`, <http://chronux.org/>)⁶⁸ from periods of spontaneous or resting behavior lasting >10 s. MUA was defined as the power between 300 and 3,000 Hz. Cross-correlations were calculated (Matlab function: `xcorr`) between the reflectance within the whisker barrel ROI and each frequency band, and then normalized by the autocorrelations. To directly compare our result against previous results obtained with interleaved electrophysiology and MRI–CBV imaging²⁰, the CBV and neural activity were both low-pass filtered below 1 Hz before calculating the cross-correlation.

Cross-correlations between heart rate and CBV were obtained during periods of rest lasting >10 s. Statistical significance was computed using bootstrap resampling⁶⁹ from 1,000 reshuffled trials.

Calculation of the hemodynamic response function. We considered the neurovascular relationship to be a linear time-invariant (LTI) system^{26,32,70}. Using this framework, a hemodynamic response function (HRF) can be calculated numerically using the relationship

$$H_{(k+1) \times 1} = (T^T T)^{-1} T^T V_{(m+k) \times 1}$$

where H is the HRF, V is the normalized and mean-subtracted CBV, and T is a Toeplitz matrix of size $(m+k) \cdot (k+1)$, containing measurements of normalized neural activity (n)

$$T(\vec{n}) = \begin{pmatrix} 1 & n_1 & 0 & 0 & \cdots & 0 \\ 1 & n_2 & n_1 & 0 & \cdots & 0 \\ \vdots & \vdots & n_2 & n_1 & \cdots & \vdots \\ \vdots & n_k & \vdots & n_2 & \cdots & n_1 \\ \vdots & 0 & n_k & \vdots & \cdots & n_2 \\ \vdots & \vdots & \vdots & n_k & \ddots & \vdots \\ 1 & 0 & 0 & 0 & \cdots & n_k \end{pmatrix}$$

For calculations of behavioral HRFs, a subtractive normalization was performed so that the period of rest prior to behavior onset had a mean equal to zero. For sensory-evoked HRFs, only neural activity within 1.5 s of the stimulus was used for calculating the HRF. For volitional whisker movement HRFs, we used a 4-s period of neural activity that began 1 s before the detected onset. This period includes any neural activity that precedes the onset of whisking or continues after superthreshold whisker movement has ceased.

HRFs were calculated from half of the data (described below) corresponding to each behavior and tested on the other half. HRFs for each behavioral dataset were calculated from gamma-band power (40–100 Hz) and MUA power (300–3,000 Hz) separately. All results were smoothed using a third-order, 11-point Savitsky–Golay filter (Matlab function: `sgolayfilt`). Note that this method makes no assumptions as to the shape of the HRF, but nonetheless we recovered the canonical gamma-distribution function shaped HRF⁷¹. HRF amplitudes in plots were scaled by a factor of 10^4 for clarity.

Comparison of HRF parameters among behaviors. Amplitude, time to peak, and full-width at half-maximum were used as parameters to compare HRFs obtained from various behaviors. The HRF for each behavior was calculated for each animal. Population means (two-way ANOVA) or medians (Friedman test) were compared to determine the significance of any differences observed in the behavior-specific HRF attributes. Bonferroni corrections were applied to correct P values for multiple comparisons in post hoc tests. The dependence of HRF attributes on cortical depth was also examined. HRF attributes across all behaviors were separated by cortical electrode depth and compared nonparametrically using a Mann–Whitney U -test.

Quantifying the variance in the CBV dynamics captured by the HRF. HRFs for each behavior were fit with a gamma-distribution function to calculate the correspondence between predicted and actual CBV. The gamma-distribution HRF was convolved with neural power to predict the measured CBV:

$$v = n \otimes h + \varepsilon$$

where v was the predicted CBV, n was the normalized neural measurements, h was the HRF, ε was the error, and \otimes denotes convolution. Data were separated into even and odd trials, spanning all imaged days. Even trials were used to generate the HRF, and odd trials were used to validate the HRFs predictions. The efficacy of the prediction was quantified by calculating the coefficient of determination (R^2) between the predicted and actual CBV:

$$R^2 = 1 - \frac{\sum (v_{\text{actual}} - v_{\text{predicted}})^2}{\sum (v_{\text{actual}} - \bar{v})^2}$$

where \bar{v} is the expected value of the measured CBV. To test the hypothesis that fluctuations in R^2 were due to behavior, R^2 values from individual and average CBV predictions were compared using the Friedman test or ANOVA, as appropriate, with Bonferroni correction for multiple comparisons in post hoc analysis.

Subtraction of the global CBV signal. To test the hypothesis that local CBV fluctuations arising from local neural activity may be obscured by a non-region-specific global signal⁷², we first obtained the global signal by averaging the reflectance over the area of the thinned-skull window. We normalized the global signal to its baseline calculated, as described above, from periods of rest and subtracted the normalized global signal from the $\Delta R/R$ within the ROI in the barrel cortex. This subtraction preserved neurovascular coupling (Fig. 1d and Supplementary Fig. 7e). We then repeated the calculation of the resting HRFs and predicted the measured reflectance after global signal subtraction (see above).

Analysis of the putatively non-neural, additive CBV signal. Data were separated according to behaviors and normalized to the resting baseline. To determine whether the hypothesized CBV component might be uncorrelated, additive noise, we compared the variance of the behavior-triggered CBV response to the variance of the CBV signal during periods of rest (Fig. 4b). Additionally, we compared the root mean squared error of the gamma-band or MUA derived HRF predictions across all behavioral conditions (Fig. 4c,d).

To examine the frequency content of the neurally uncorrelated CBV component, the predicted CBV signal was subtracted from the measured CBV during periods of rest, and the multitapered power spectral density of the residuals were calculated (Matlab Chronux toolbox version 2.11 function: `mtspectrum`; <http://chronux.org/>)⁶⁸ for each animal.

Statistics. Before statistical testing, sample populations were tested for normality (Anderson–Darling test, Matlab function: `adtest`). If the distribution was not normal, the median \pm interquartile range was used to describe distributions instead of mean \pm standard deviation. For comparisons of multiple populations, the assumption of equal variance needed for parametric was also tested (two sample F -test, Matlab function: `vartest2`; or Bartlett test, Matlab function: `vartestn`). If the conditions of normality and equal variance were not met, parametric

tests (*t* test, paired *t* test, Welch's *t* test, one-way ANOVA, or two-way ANOVA) were substituted with a nonparametric counterpart (Mann–Whitney *U*-test, Wilcoxon signed-rank test, Kruskal–Wallis ANOVA, or Friedman test). Wherever appropriate, we accounted for within-subject variations using paired tests, two-factor ANOVA/Friedman tests, or mixed-effects modeling⁷³ (Matlab function: fitlme). Where $n > 10$, the approximate method of Wilcoxon signed-rank testing was used, because signed ranks have a normal distribution; otherwise the exact sums of the signed ranks were used. All statistical comparisons were two-sided tests unless otherwise noted. Confidence intervals were obtained from bootstrap resampling (Matlab function: bootci; 1,000 resamples) from statistics calculated on randomly reshuffled data, where the size of the reshuffled dataset was equal to the original dataset.

Code availability. Code used to generate the figures in this paper is available at https://github.com/DrewLab/Winder_Echagarruga_Zhang_Drew_2017_Code.

Data availability. The data in this paper are available at <https://psu.app.box.com/v/Winder2017-Code-Data>.

References

51. Drew, P. J. et al. Chronic optical access through a polished and reinforced thinned skull. *Nat. Methods* **7**, 981–984 (2010).
52. Drew, P. J. & Feldman, D. E. Intrinsic signal imaging of deprivation-induced contraction of whisker representations in rat somatosensory cortex. *Cereb. Cortex* **19**, 331–348 (2009).
53. Shirey, M. J. et al. Brief anesthesia, but not voluntary locomotion, significantly alters cortical temperature. *J. Neurophysiol.* **114**, 309–322 (2015).
54. Gehrmann, J. et al. Phenotypic screening for heart rate variability in the mouse. *Am. J. Physiol. Heart Circ. Physiol.* **279**, H733–H740 (2000).
55. Huo, B.-X., Greene, S. E. & Drew, P. J. Venous cerebral blood volume increase during voluntary locomotion reflects cardiovascular changes. *Neuroimage* **118**, 301–312 (2015).
56. O'Connor, S. M., Berg, R. W. & Kleinfeld, D. Coherent electrical activity between vibrissa sensory areas of cerebellum and neocortex is enhanced during free whisking. *J. Neurophysiol.* **87**, 2137–2148 (2002).
57. Ganguly, K. & Kleinfeld, D. Goal-directed whisking increases phase-locking between vibrissa movement and electrical activity in primary sensory cortex in rat. *Proc. Natl. Acad. Sci. USA* **101**, 12348–12353 (2004).
58. Henze, D. A. et al. Intracellular features predicted by extracellular recordings in the hippocampus in vivo. *J. Neurophysiol.* **84**, 390–400 (2000).
59. Drew, P. J., Blinder, P., Cauwenberghs, G., Shih, A. Y. & Kleinfeld, D. Rapid determination of particle velocity from space-time images using the Radon transform. *J. Comput. Neurosci.* **29**, 5–11 (2010).
60. Gao, Y.-R. & Drew, P. J. Effects of voluntary locomotion and calcitonin gene-related peptide on the dynamics of single dural vessels in awake mice. *J. Neurosci.* **36**, 2503–2516 (2016).
61. Zhao, X., Chen, H., Liu, X. & Cang, J. Orientation-selective responses in the mouse lateral geniculate nucleus. *J. Neurosci.* **33**, 12751–12763 (2013).
62. Constantinople, C. M. & Bruno, R. M. Effects and mechanisms of wakefulness on local cortical networks. *Neuron* **69**, 1061–1068 (2011).
63. Napoleone, P., Erdö, S. & Amenta, F. Autoradiographic localization of the GABAA receptor agonist [3H]muscimol in rat cerebral vessels. *Brain Res.* **423**, 109–115 (1987).
64. de Blas, A. L., Vitorica, J. & Friedrich, P. Localization of the GABAA receptor in the rat brain with a monoclonal antibody to the 57,000 Mr peptide of the GABAA receptor/benzodiazepine receptor/Cl⁻ channel complex. *J. Neurosci.* **8**, 602–614 (1988).
65. Lein, E. S. et al. Genome-wide atlas of gene expression in the adult mouse brain. *Nature* **445**, 168–176 (2007).
66. Anenberg, E., Chan, A. W., Xie, Y., LeDue, J. M. & Murphy, T. H. Optogenetic stimulation of GABA neurons can decrease local neuronal activity while increasing cortical blood flow. *J. Cereb. Blood Flow Metab.* **35**, 1579–1586 (2015).
67. Gao, Y.-R. & Drew, P. J. Determination of vessel cross-sectional area by thresholding in Radon space. *J. Cereb. Blood Flow Metab.* **34**, 1180–1187 (2014).
68. Mitra, P. & Bokil, H. *Observed Brain Dynamics* (Oxford University Press, 2008).
69. Hutchison, R. M. et al. Dynamic functional connectivity: promise, issues, and interpretations. *Neuroimage* **80**, 360–378 (2013).
70. Glover, G. H. Deconvolution of impulse response in event-related BOLD fMRI. *Neuroimage* **9**, 416–429 (1999).
71. de Zwart, J. A. et al. Temporal dynamics of the BOLD fMRI impulse response. *Neuroimage* **24**, 667–677 (2005).
72. Pisuro, M. A., Benucci, A. & Carandini, M. Local and global contributions to hemodynamic activity in mouse cortex. *J. Neurophysiol.* **115**, 2931–2936 (2016).
73. Aarts, E., Verhage, M., Veenliet, J. V., Dolan, C. V. & van der Sluis, S. A solution to dependency: using multilevel analysis to accommodate nested data. *Nat. Neurosci.* **17**, 491–496 (2014).
74. Mateo, C. I., Knutsen, P. M., Tsai, P. S., Shih, A. Y. & Kleinfeld, D. Neuron <https://dx.doi.org/10.1016/j.neuron.2017.10.012> (2017).

Life Sciences Reporting Summary

Nature Research wishes to improve the reproducibility of the work that we publish. This form is intended for publication with all accepted life science papers and provides structure for consistency and transparency in reporting. Every life science submission will use this form; some list items might not apply to an individual manuscript, but all fields must be completed for clarity.

For further information on the points included in this form, see [Reporting Life Sciences Research](#). For further information on Nature Research policies, including our [data availability policy](#), see [Authors & Referees](#) and the [Editorial Policy Checklist](#).

▶ Experimental design

1. Sample size

Describe how sample size was determined.

Sample sizes were chose to be consistent with previous studies.

2. Data exclusions

Describe any data exclusions.

Auditory and ipsilateral stimuli were administered but omitted from the primary analysis because their responses were primarily related to stimulus-provoked movement, see figure S1h.

Animals which did not show reduced neural activity following pharmacological infusion were not analyzed.

Data taken during periods of behavioral transitioning were omitted from analysis.

For infusion experiments all data taken after any aberrant neural activity or CBV were omitted from analysis.

Three animals were omitted from the comparison of the infusion ROI to the rest of the window (S10) since their windows were mostly spanned by the radius of the CBV ROI.

3. Replication

Describe whether the experimental findings were reliably reproduced.

All animals showed similar hemodynamic response function dynamics.

All animals showed a low agreement between the predicted and measured CBV during periods of rest.

All animals with reduced MUA following pharmacological infusions showed a substantial continuing CBV oscillation within the region of interest

4. Randomization

Describe how samples/organisms/participants were allocated into experimental groups.

Infusion orders were counter-balanced so all mice received all treatments in alternating orders to mitigate effects of imaging sessions on one treatment, therefore no randomization was performed.

5. Blinding

Describe whether the investigators were blinded to group allocation during data collection and/or analysis.

Experimenters were not blinded to cranial nerve transection experiments.

No blinding took place during pharmacological infusion experiments since the experimental design was a crossed-over, so that animals received both a treatment and control infusion in a counterbalanced order. Analysis of the data was performed using an automated analysis script with minimal experimenter input.

Note: all studies involving animals and/or human research participants must disclose whether blinding and randomization were used.

6. Statistical parameters

For all figures and tables that use statistical methods, confirm that the following items are present in relevant figure legends (or in the Methods section if additional space is needed).

n/a Confirmed

- The exact sample size (n) for each experimental group/condition, given as a discrete number and unit of measurement (animals, litters, cultures, etc.)
- A description of how samples were collected, noting whether measurements were taken from distinct samples or whether the same sample was measured repeatedly
- A statement indicating how many times each experiment was replicated
- The statistical test(s) used and whether they are one- or two-sided (note: only common tests should be described solely by name; more complex techniques should be described in the Methods section)
- A description of any assumptions or corrections, such as an adjustment for multiple comparisons
- The test results (e.g. P values) given as exact values whenever possible and with confidence intervals noted
- A clear description of statistics including central tendency (e.g. median, mean) and variation (e.g. standard deviation, interquartile range)
- Clearly defined error bars

See the web collection on [statistics for biologists](#) for further resources and guidance.

► Software

Policy information about [availability of computer code](#)

7. Software

Describe the software used to analyze the data in this study.

Custom code written in MATLAB 2015a was used to analyze the data and is available for download.

For manuscripts utilizing custom algorithms or software that are central to the paper but not yet described in the published literature, software must be made available to editors and reviewers upon request. We strongly encourage code deposition in a community repository (e.g. GitHub). [Nature Methods guidance for providing algorithms and software for publication](#) provides further information on this topic.

► Materials and reagents

Policy information about [availability of materials](#)

8. Materials availability

Indicate whether there are restrictions on availability of unique materials or if these materials are only available for distribution by a for-profit company.

N/A

9. Antibodies

Describe the antibodies used and how they were validated for use in the system under study (i.e. assay and species).

N/A

10. Eukaryotic cell lines

a. State the source of each eukaryotic cell line used.

N/A

b. Describe the method of cell line authentication used.

N/A

c. Report whether the cell lines were tested for mycoplasma contamination.

N/A

d. If any of the cell lines used are listed in the database of commonly misidentified cell lines maintained by [ICLAC](#), provide a scientific rationale for their use.

N/A

► Animals and human research participants

Policy information about [studies involving animals](#); when reporting animal research, follow the [ARRIVE guidelines](#)

11. Description of research animals

Provide details on animals and/or animal-derived materials used in the study.

Mice were male C57-BJ6 acquired from Jackson Laboratory and were used between the ages of 3-8 months




12. Description of human research participants

Describe the covariate-relevant population characteristics of the human research participants.

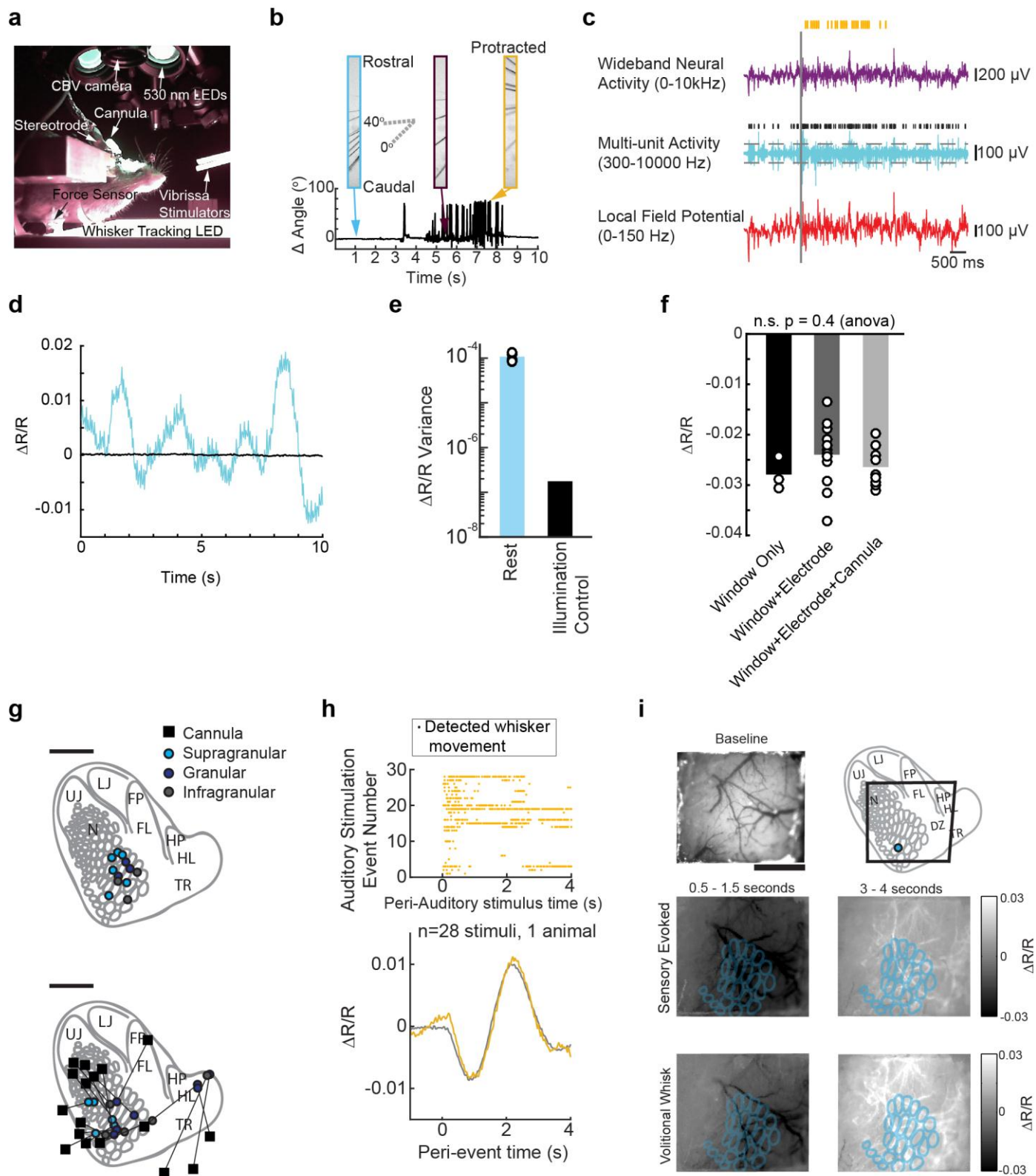
N/A

In the format provided by the authors and unedited.

Weak correlations between hemodynamic signals and ongoing neural activity during the resting state

Aaron T. Winder^{1,2}, Christina Echagarruga ^{1,3}, Qingguang Zhang ^{1,2} and Patrick J. Drew ^{1,2,3,4*}

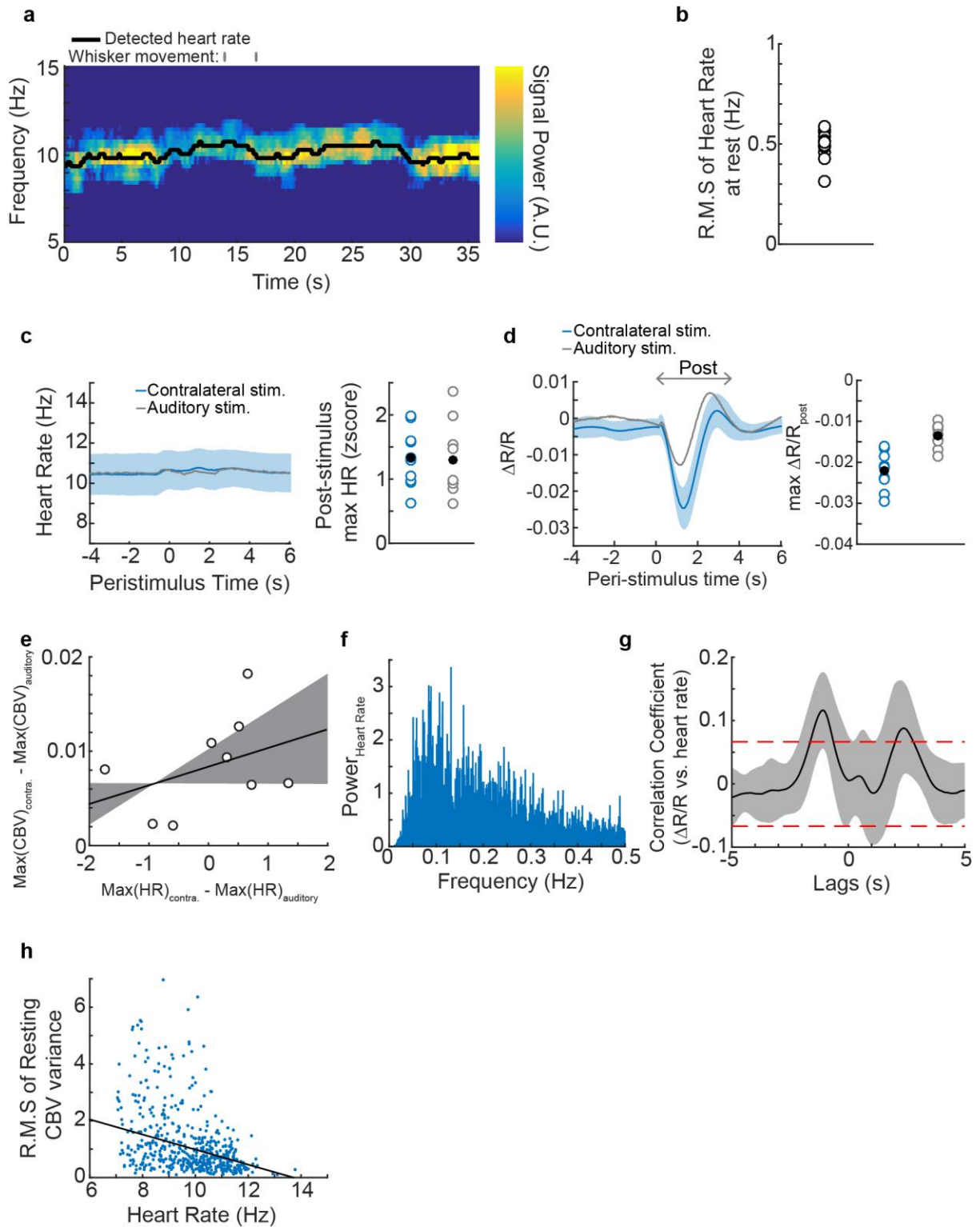
¹Center for Neural Engineering, Pennsylvania State University, University Park, PA, USA. ²Department of Engineering Science and Mechanics, Pennsylvania State University, University Park, PA, USA. ³Graduate Program in Bioengineering, Pennsylvania State University, University Park, PA, USA. ⁴Department of Neurosurgery and Department of Biomedical Engineering, Pennsylvania State University, University Park, PA, USA. *e-mail: pjd17@psu.edu



Supplementary Figure 1

Details of the experimental model.

a: Photo of the experimental setup showing an awake, head-fixed mouse. The stereotrode and cannula are visible on the head. b: An example of the automated detection of whisker angle. Images of the whiskers at various times are indicated by colored boxes and arrows. The light blue box shows the whiskers at rest. The purple and orange boxes show the whiskers at various positions during volitional movement. c: An example of neural data during sensory stimulation (vertical gray bar) and the subsequent whisking (orange tick marks) showing wideband neural activity (0-10 kHz), multi-unit activity (300-3000 Hz), and local field potentials (0-150 Hz). Individual spikes (black tick marks, >5 standard deviations threshold shown with horizontal dashed lines) were detected in all animals. d: An example of the resting CBV signal (blue) compared to the reflectance obtained from a piece of clay placed over the cranial window during an experimental session (black). This shows the instrumentation noise is minuscule compared to the CBV signal. e: A comparison of the resting variance to the variance measured from the occluded cranial window which served as an illumination control surface. The variance of the instrumentation noise was 0.16% of the mean resting variance across all animals (n=12). f: A comparison of the mean CBV amplitude changes following contralateral whisker stimulation between animals with only implanted electrodes (n=12) or cannula and electrodes (n=9) and animals with no implants (n=3). The circles show individual animals. Bars show the mean of each group. The sensory-evoked CBV response was not affected by implantation of stereotrodes or cannulas (One-way ANOVA, $n=\{3,12,9\}$, $p=0.40$, $F(2,23)=0.95$). g: A reconstruction of the position and depth of implanted stereotrodes (colored circles) and the position of cannulas (black squares) for all animals. Stereotrode depths are designated by color. Scale bar = 1mm. h: Whisking and CBV response to auditory stimuli for a representative animal. Auditory stimuli elicited volitional whisking behaviors, which then drove a hemodynamic response. Top: 28 examples of the detected whisker movements following auditory stimulation. Bottom: the average measured reflectance following auditory stimuli and compared to the response following volitional whisking without any stimulus. See Figure 1e, for population comparison of behavioral CBV variance. i: Averaged reflectance changes relative to baseline (top left) for a representative animal in response to a contralateral whisker stimulation (middle row) and during volitional whisking (bottom row). Brightness shows the mean normalized reflectance change from baseline. The light blue circular regions show the positions of individual macro-vibrissae barrel reconstructed from layer IV cytochrome oxidase staining. The locations of the implanted stereotrode (blue filled circle) and sensory regions are shown (top right). UJ: upper jaw, LJ: lower jaw, N: nose, FP: forepaw, FL: forelimb, HP: hindpaw, HL: hindlimb, TR: trunk, DZ: dysgranular zone. Scale bars = 1 mm.

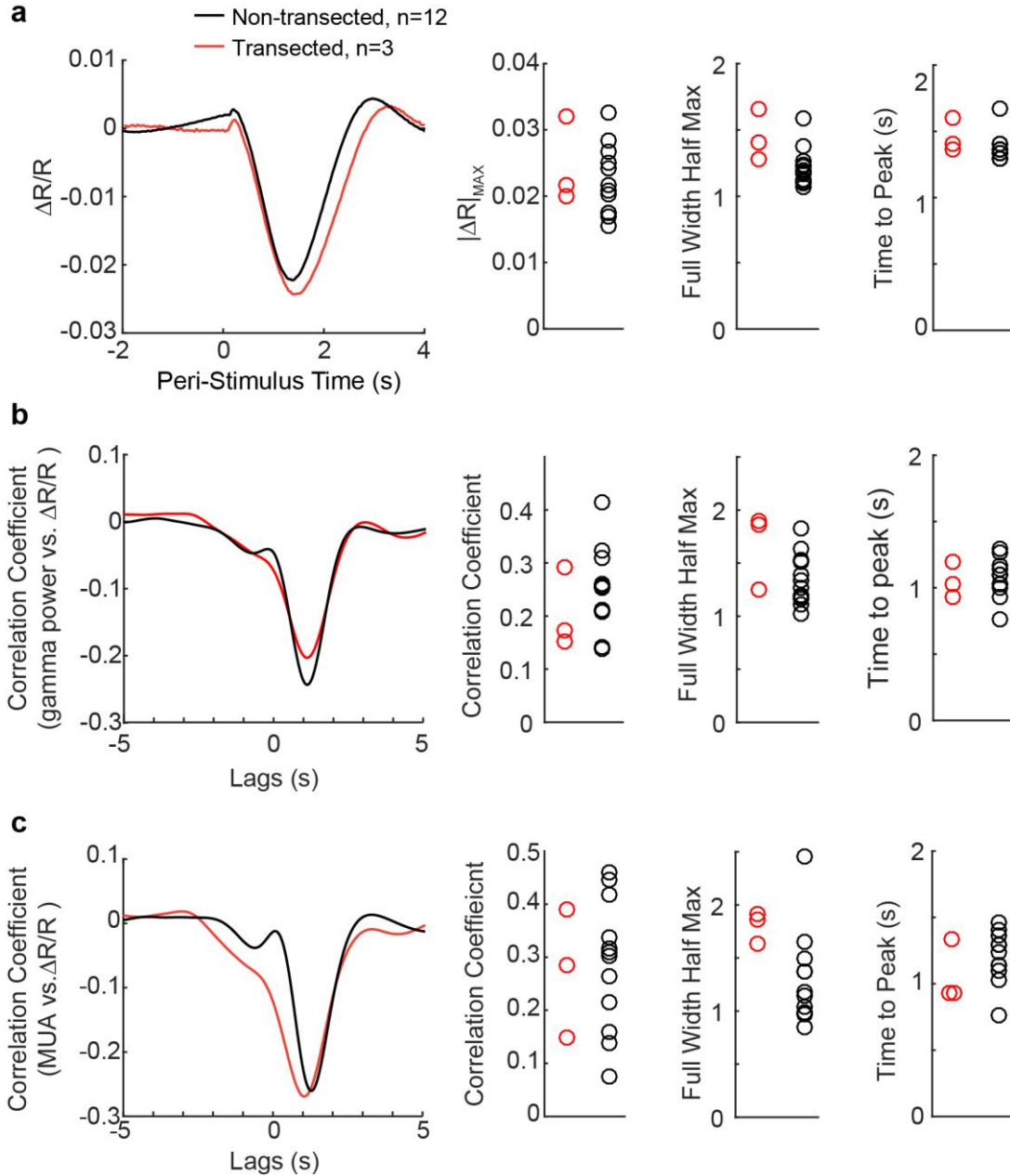


Supplementary Figure 2

Heart-rate fluctuations are poorly correlated with sensory-evoked and spontaneous resting CBV changes.

a: Example of heart-rate fluctuations from a ~35-second-long period of rest. b: A scatterplot showing the root mean squared amplitude of heart rate fluctuations at rest for all animals ($n=12$). c: The stimulus-triggered average heart rate among animals shows a small heart

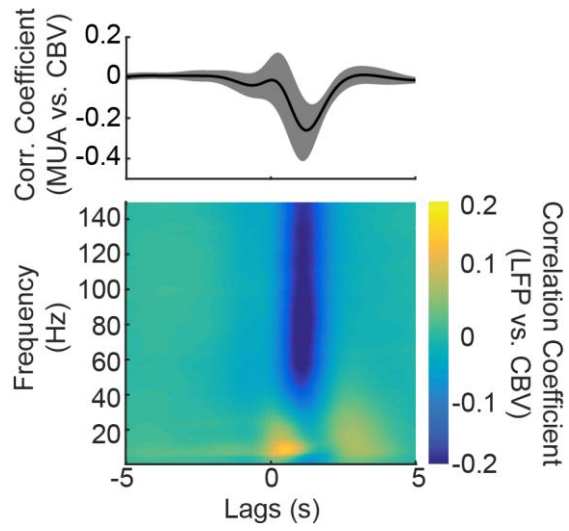
rate increase following contralateral ($n=9$, $\text{mean}\pm\text{std}:2.2\pm1.3\%$, blue, shaded region indicates standard deviation) and auditory ($\text{mean}\pm\text{std}:0.4\pm1.6\%$, gray) stimulation. The peak heart rate for each animal (circles) is plotted to the right. Black circles indicate the mean of all animals. The heart rate increase following contralateral stimulation was not significantly larger than increases following an auditory stimulus (paired t-test, $p=0.92$, $t(8)=0.11$, $n=9$). d: A comparison of the average stimulus-triggered reflectance changes driven by contralateral and auditory stimuli (solid blue and gray traces, respectively, shaded region shows the standard deviation). The contralateral puff elicited a larger CBV response than the auditory stimulus (blue, gray circles, paired t-test, $p=1\times10^{-3}$, $t(8)=-5.06$). e: There was no significant linear relationship between CBV and heart rate increases following whisker and auditory stimuli in the data shown in c and d ($n=9$, iteratively reweighted least squares, bisquare weighting, MATLAB function: `robustfit`, slope 0.002 ± 0.002 ($\text{mean}\pm\text{standard error}$), $p=0.35$, $t(7)=0.99$). Each animal is represented by a circle, fitted line shown as solid gray line, standard error is shown by shaded region and includes the zero slope. f: The power spectral density of the heart rate during periods of rest, averaged over all animals ($n=12$). g: The mean cross-correlation between heart rate and CBV. Shaded region shows the standard deviation across animals ($n=12$). The dashed red lines represent the 95% confidence interval based on reshuffled data (bootstrap, MATLAB function: `bootci`, 1000 resamples). h: A pooled scatter plot of the mean heart rate and root mean squared (R.M.S.) CBV during individual periods of rest (colored points) for all animals. Black line shows the linear fit using linear mixed-effects regression. There was a significant relationship between heart rate and the amplitude of the resting CBV variance ($p=0.004$, $t(532)=-2.9$) but this relationship only explained 12.5% of differences in resting CBV variance ($R^2=0.125$).



Supplementary Figure 3

Neurovascular coupling in facial-nerve-transected animals.

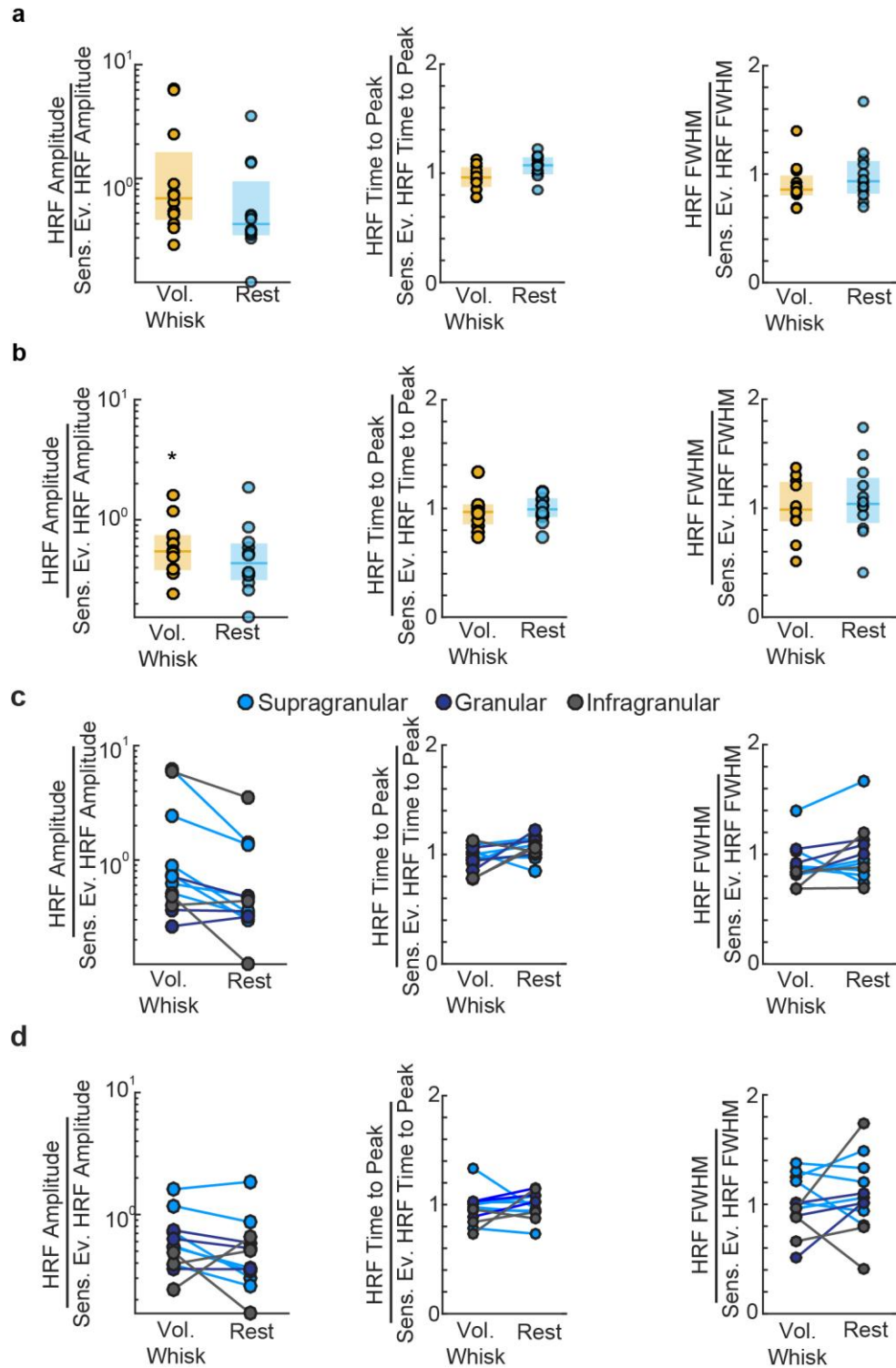
a: A comparison of the mean stimulus triggered average CBV between animals with facial nerve transections (red, $n=3$) and intact animals (black, $n=12$) (left). Statistical comparison of the responses shows no significant difference between the response amplitudes (middle left, unpaired t-test, $p=0.52$, $t(13)=0.66$), full-width at half-max (middle right, unpaired t-test, Bonferroni corrected, $p=0.12$, $t(13)=2.33$), and the time to peak response (right, unpaired t-test, $p=0.24$, $t(13)=1.24$). Circles show results from individual animals. b: The mean cross-correlation between gamma-band neural power and $\Delta R/R$ during non-sensory evoked behavior for animals with facial nerve transections (red, $n=3$) and intact animals (black, $n=12$) (left). There were no significant difference in the maximum correlation coefficients between gamma-band power and normalized reflectance (middle left, unpaired t-test, $p=0.41$, $t(13)=-0.86$), width of the cross correlation (middle right, unpaired t-test, $p=0.08$, $t(13)=-1.92$), or the lag at maximum correlation (right, unpaired t-test, $p=0.81$, $t(13)=0.24$) compared between mice with intact facial nerves (black circles) and mice with transected facial nerves (red circles). c: same as b, but for the correlation between MUA and $\Delta R/R$. (Unpaired t-test, Max correlation coefficient: $p=0.88$, $t(13)=-0.16$; FWHM: $p=0.07$, $t(13)=-1.95$; Time to peak: $p=0.31$, $t(13)=1.05$)



Supplementary Figure 4

Spontaneous cross-correlation between the LFP and reflectance in the barrel cortex in the absence of sensory stimulation.

Top: cross-correlation between MUA power and $\Delta R/R$ during all periods without whisker stimulation. The shaded region shows the population standard deviation (n=12). Bottom: cross-correlation between $\Delta R/R$ and various frequency bands of the LFP. Color bar shows the magnitude of the correlations.



Supplementary Figure 5

Attributes of gamma-band power and MUA HRFs.

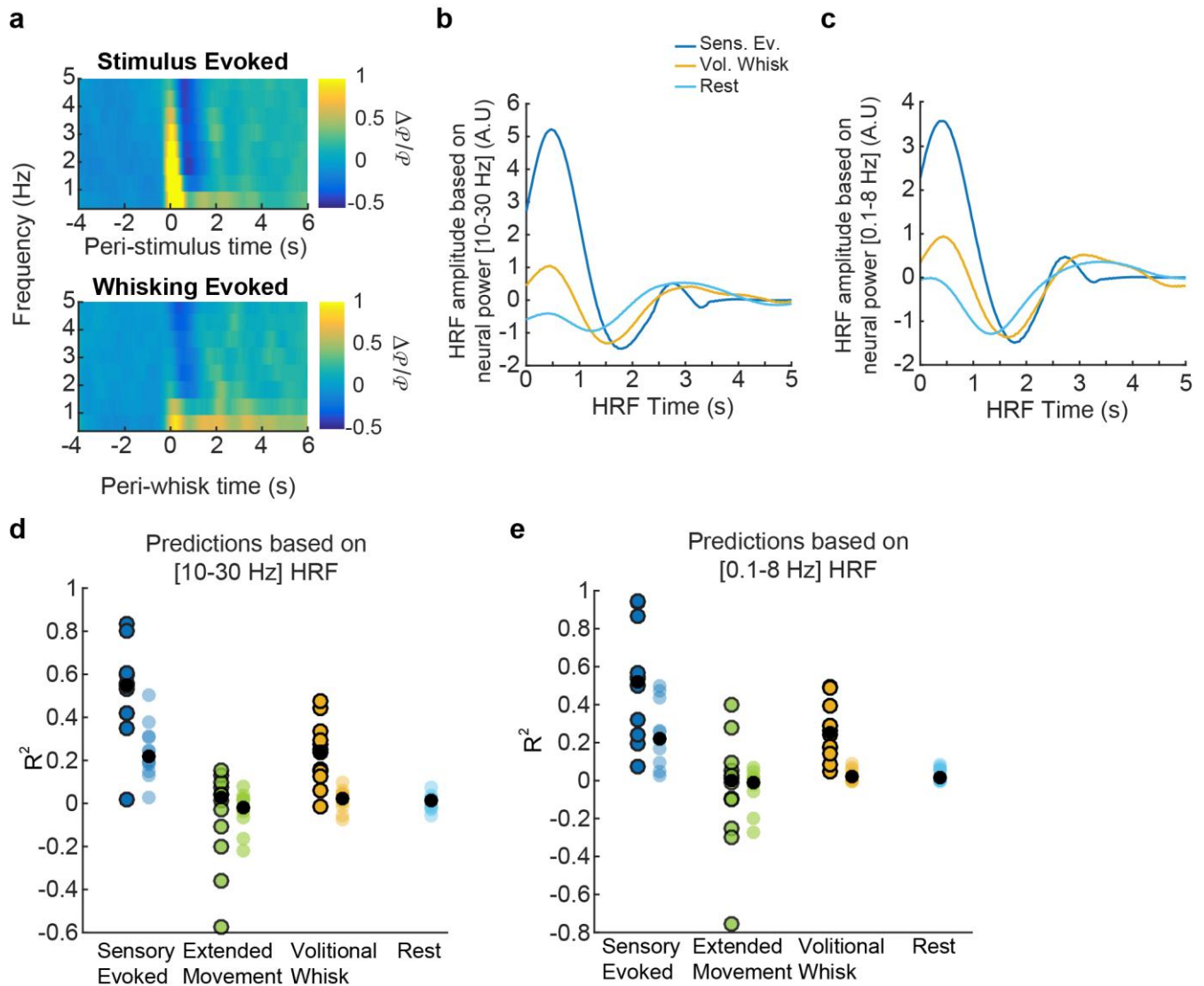
a: The amplitude, time to peak (TTP) and full-width at half-max (FWHM) of the gamma-band derived HRFs. Each circle represents the attribute from a single animal (n=12) normalized by the sensory-evoked HRF

attribute. Horizontal bars and shaded boxes show the median and interquartile range, respectively (amplitude comparison: Wilcoxon signed rank, Bonferroni corrected, stimulation vs. whisking: $p=0.64$, $z=-0.47$, stimulation vs. rest: $p=0.06$, $z=-1.88$. Time to peak comparison: paired t-test, stimulation vs. whisking: $p=0.23$, $t(11)=-1.28$; stimulation vs. rest: $p=0.06$, $t(11)=2.09$. Full-width-half-maximum comparison: paired t-test, Bonferroni corrected, stimulation vs whisking: $p=0.11$, $t(11)=-1.74$, Stimulation vs rest: $p=0.95$, $t(11)=-0.07$).

b: Same as **a** but for HRFs calculated from MUA power. (amplitude comparison: Wilcoxon signed rank, Bonferroni corrected, stimulation vs. whisking: $p=0.05$, $z=-2.27$, stimulation vs. rest: $p=0.07$, $z=-2.12$. Time to peak: Paired t-test, stimulation vs. whisking: $p=0.41$, $t(11)=-0.86$; stimulation vs. rest: $p=0.80$, $t(11)=-0.26$. Full-width-half-maximum comparison: paired t-test, stimulation vs. whisking: $p=0.97$, $t(11)=0.04$; stimulation vs. rest: $p=0.47$, $t(11)=0.75$).

c: The attributes of the gamma-band derived HRF categorized according to stereotrode depth. Colored circles denote the depth of the implanted stereotrode obtained from histological reconstructions of each animal (Supragranular: $n=6$, Granular: $n=3$, Infragranular: $n=3$). There was no detectable dependency of HRF attributes on the cortical depth of the recording site.(HRF amplitude: Mann-Whitney U Test, Supragranular vs. granular: $p=0.07$, $z=1.83$, supragranular vs. infragranular: $p=0.74$, $z=0.33$, granular vs. infragranular: $p=0.30$, $z=-1.04$; HRF time to peak: unpaired t-test, supragranular vs. granular: $p=0.81$, $t(16)=-0.38$, supragranular vs. infragranular: $p=0.53$, $t(16)=-0.64$, granular vs. infragranular: $p=0.51$, $t(10)=0.69$; HRF FWHM: Mann-Whitney U-test, supragranular vs. granular: $p=0.21$, $z=-1.26$, supragranular vs. infragranular: $p=0.15$, $z=1.45$; granular vs. infragranular: $p=0.13$, $z=-1.52$)

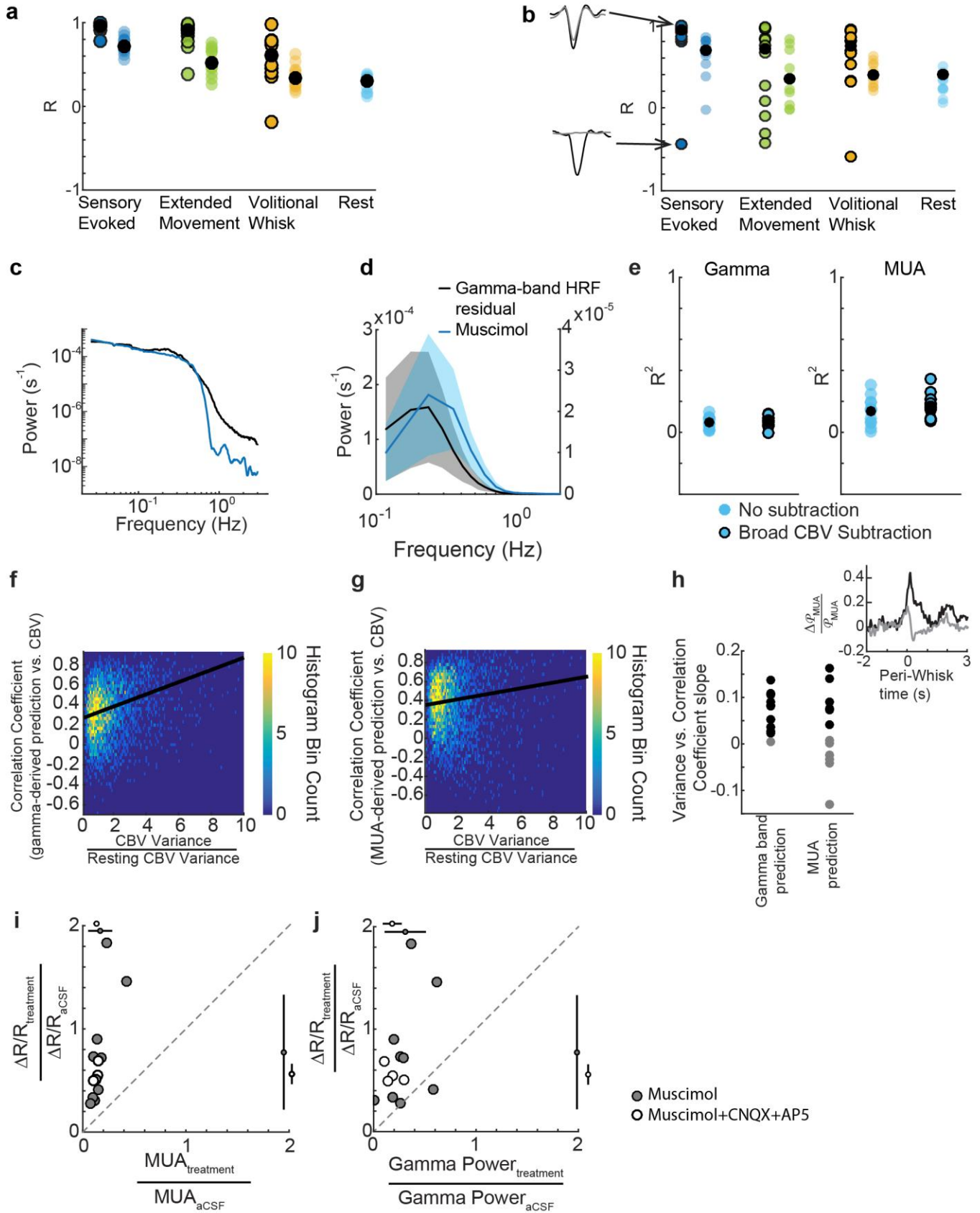
d: Same as **c**, but for MUA derived HRF attributes (HRF amplitude: Mann-Whitney U-test, supragranular vs. granular: $p=0.81$, $z=0.23$, supragranular vs. infragranular: $p=0.21$, $z=1.26$, granular vs. infragranular: $p=0.30$, $z=-1.04$; HRF TTP: unpaired t-test, supragranular vs. granular: $p=0.39$, $t(16)=-0.87$, supragranular vs. infragranular: $p=0.39$, $t(16)=-0.88$, granular vs. infragranular: $p=0.10$, $t(10)=-1.83$; HRF FWHM: Mann-Whitney U-test, supragranular vs. granular: $p=0.07$, $z=1.83$; supragranular vs. infragranular: $p=0.07$, $z=1.83$, granular vs. infragranular: $p=0.30$, $z=1.04$).



Supplementary Figure 6

HRFs calculated from lower frequencies of the LFP.

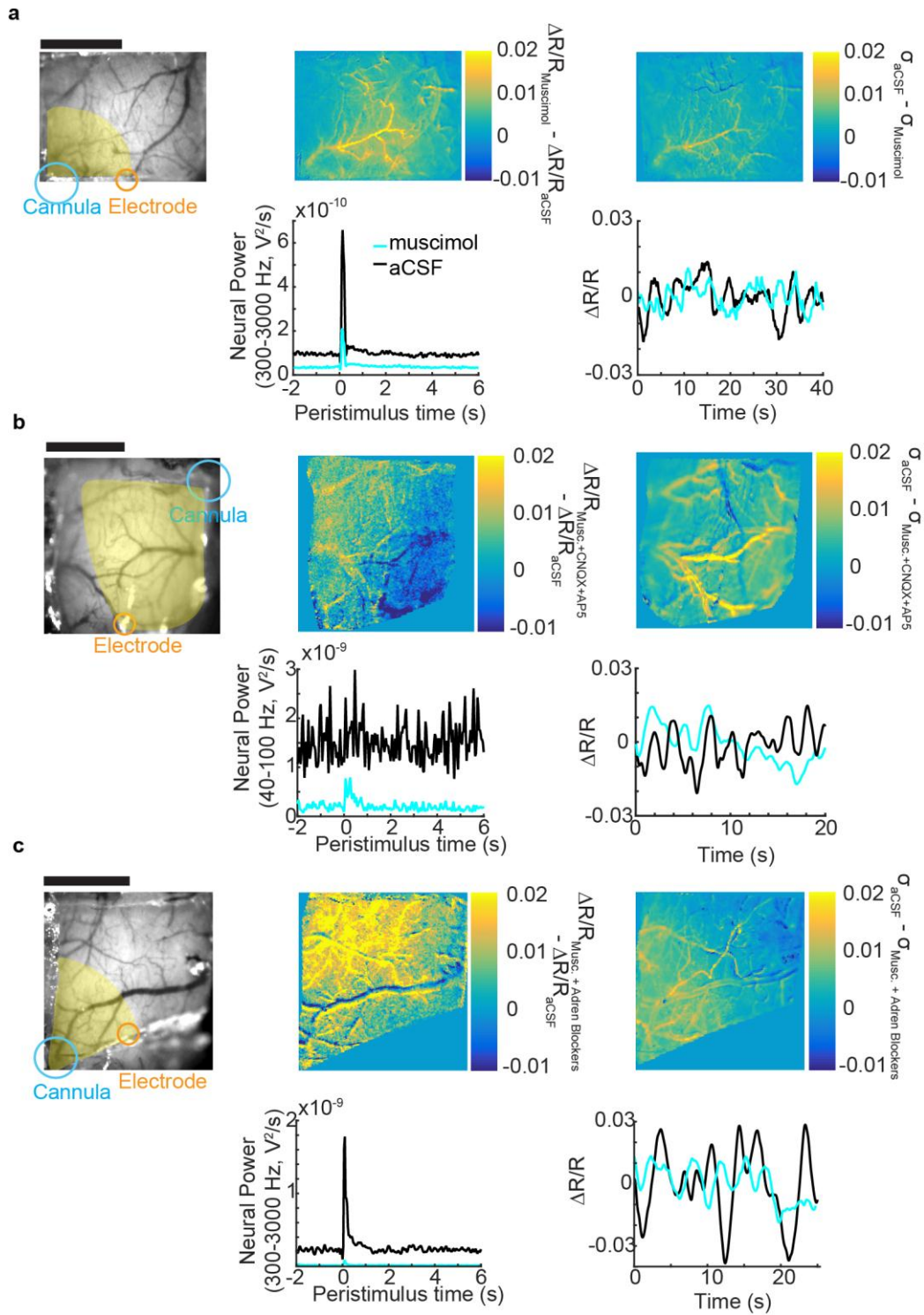
a: Mean stimulus (top) and whisking (bottom) triggered neural power in the LFP at frequencies below 5 Hz ($n=12$). **b:** A comparison of the mean HRFs derived from neural power in the 10-30 Hz band. Each HRF was calculated from a single behavioral state: stimulation (dark blue), volitional whisking (orange), and rest (light blue) and averaged across animals ($n=12$). **c:** Same as b, but calculated from neural power in the 0.1-8 Hz band. **d:** Population summary of the goodness of fit (R^2) of the CBV predictions based on neural power in the 10-30 Hz band. Circles represent median R^2 for each animal. R^2 calculated on predictions of the average behavior-triggered CBV are outlined in black, filled black circles show the population medians (Rest: $R^2=0.015$). Circles without black outlines show medians of predictions from individual trials. **e:** Same as **d**, but for HRFs calculated from neural power in the 0.1-8 Hz. The median R^2 of predictions using the 0.1-8 Hz band of the LFP of resting CBV was 0.018.



Supplementary Figure 7

Additional analyses of the CBV signal.

a: Population summary of the correlation between gamma-band power derived CBV predictions and measured CBV, separated according to behavior. Circles represent median correlation coefficient (R) for each animal (n=12). R values calculated using predictions of the average behavior-triggered CBV are outlined in black (Friedman test, $p=1 \times 10^{-4}$, $\chi^2(2,22) = 18.5$. Post-hoc: Wilcoxon signed rank with Bonferroni correction, sensory evoked vs. extended movement: $p=0.18$, $z=1.88$; sensory evoked vs. volitional whisking: $p=6 \times 10^{-3}$, $z=3.06$; extended movement vs. volitional whisking: $p=0.08$, $z=2.20$). The other colored circles indicate the median R values calculated for predictions of CBV during individual periods of behavior, (Two-way ANOVA, $p=9 \times 10^{-12}$, $F(3,11)=45.01$. Post-hoc: paired t-test with Bonferroni correction. sensory evoked vs. extended movement: $p=0.01$, $t(11)=3.81$; sensory evoked vs. volitional whisking: $p=6 \times 10^{-5}$, $t(11)=7.15$, sensory evoked vs. rest: $p=6 \times 10^{-7}$, $t(11)=11.40$, extended movement vs. volitional whisking: $p=1 \times 10^{-3}$, $t(11)=5.11$, volitional whisking vs. rest: $p=0.13$, $t(11)=2.29$, extended movement vs. rest: $p=1 \times 10^{-4}$, $t(11)=6.46$). The filled black circles indicate the population medians. b: Same as in a, but corresponding to MUA-derived HRFs (Averaged CBV: Friedman Test, $p=0.04$, $\chi^2(2,22)=6.5$, Post-hoc: Wilcoxon signed-rank with Bonferroni correction, sensory-evoked vs. extended movement: $p=0.08$, $z=2.19$, sensory-evoked vs. volitional whisk: $p=0.12$, $z=2.04$, volitional whisk vs. rest: $p=0.4$, $t(11)=-0.86$; Individual CBV: Friedman test, $p=4 \times 10^{-3}$, $\chi^2(3,33)=13.2$, Post-hoc: Wilcoxon signed rank with Bonferroni correction, sensory evoked vs. extended movement: $p=0.05$, $z=2.67$, sensory evoked vs. volitional whisk: $p=0.05$, $z=2.59$, sensory evoked vs. rest: $p=0.09$, $z=2.43$, extended movement vs. whisk: $p=0.39$, $z=-0.86$, extended movement vs. rest: $p=0.81$, $z=-0.23$, volitional whisk vs. rest: $p=0.53$, $z=0.63$). Inset waveforms show examples of average sensory-evoked predictions (gray) with high and low correlations to the measured CBV (black). c: Example power spectra of the measured (black) and predicted (blue) CBV over all trials for a single animal. d: The mean power of the resting CBV prediction residuals (using the gamma-band HRF) across all animals (n=12, black line). For comparison, the mean resting power spectrum following infusion of muscimol was also plotted (n=9, blue line) was also plotted (see right axis for scale). Shaded regions indicate the population standard deviations. e: Subtraction of the global CBV signal did not substantially improve the gamma-band (paired t-test, $p=0.39$, $t(11)=0.90$) or MUA derived (Paired t-test, $p=0.03$, $t(11)=2.87$) prediction of CBV at rest. Colored circles denote single animals (n=12). Black-filled circles indicate the mean. f: A 2-dimensional histogram of correlation coefficients between the gamma-band power derived predictions and the measured CBV during periods of spontaneous behavior, pooled across all animals, and the normalized CBV variance from the same period. Black line shows the best fit line (Linear mixed-effects regression, $p=1.44 \times 10^{-8}$, $t(3420)=5.68$) g: same as f, but for MUA derived CBV predictions (Linear mixed-effects regression, $p=0.17$, $t(3420)=1.35$). h: Slopes from f and g plotted for each animal. Slopes which were significantly different from zero ($p < 0.05$) are black, all others are gray. The average MUA response to whisking was compared between animals with significant and not significant slopes showing differences in the whisking triggered MUA between the groups (inset). i: The changes in **sensory-evoked summed MUA power and CBV (circles)**. Circles and bars outside the axes show the mean and standard deviation of each measure. We observed an $86 \pm 3\%$ reduction in MUA standard deviation compared to aCSF controls and an $87 \pm 2\%$ reduction following muscimol+CNQX+AP5 infusions, sensory evoked CBV were reduced $23 \pm 55\%$ and $44 \pm 9\%$ respectively. The reduction in CBV response to sensory stimulation was not significantly different between muscimol and muscimol+CNQX+AP5 (Welch's t-test, $p=0.15$, $t(4.5)=1.13$). j: Same as for i, except for measured of **summed gamma-band power following stimulation**. Sensory-evoked gamma-band power was reduced $69 \pm 19\%$ following infusion of muscimol and $82 \pm 8\%$ following infusion of muscimol+CNQX+AP5 (unpaired t-test, one-sided, $p=0.12$, $t(11)=1.24$).

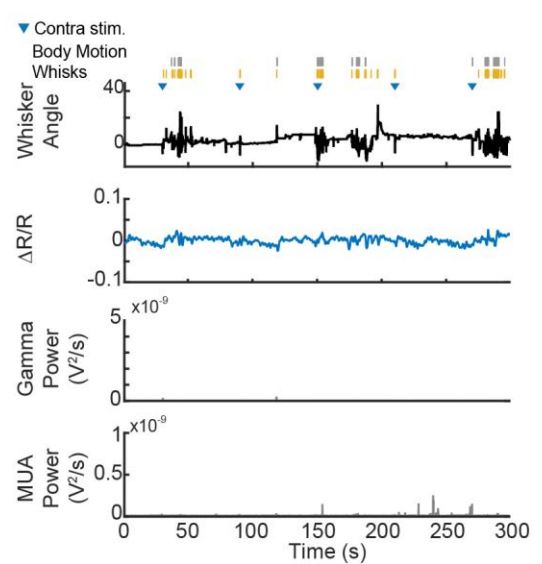
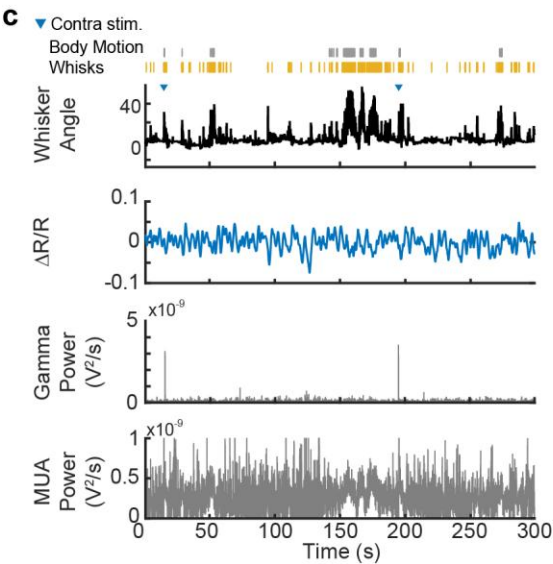
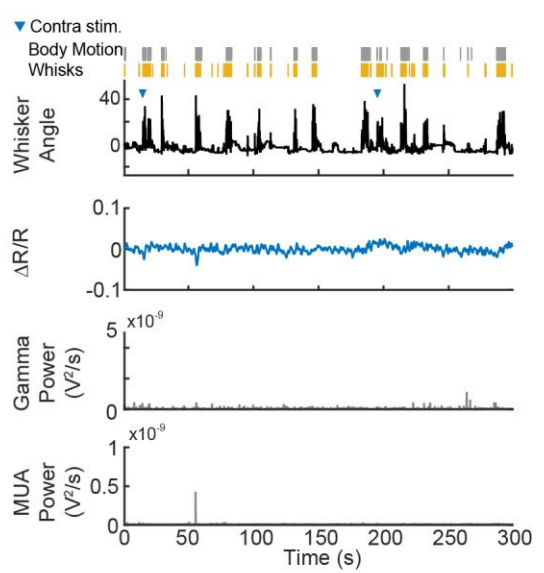
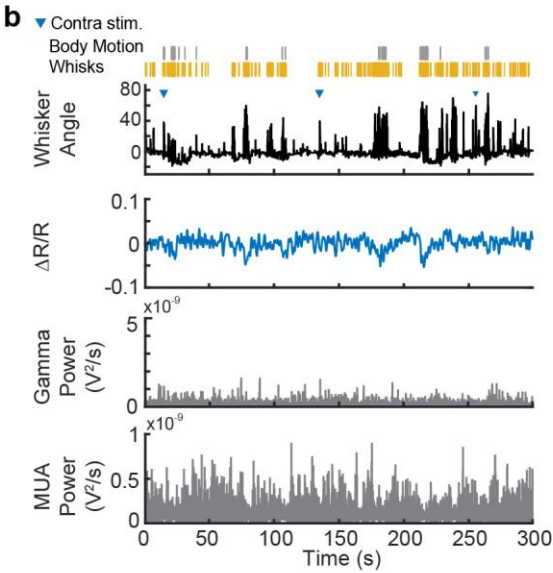
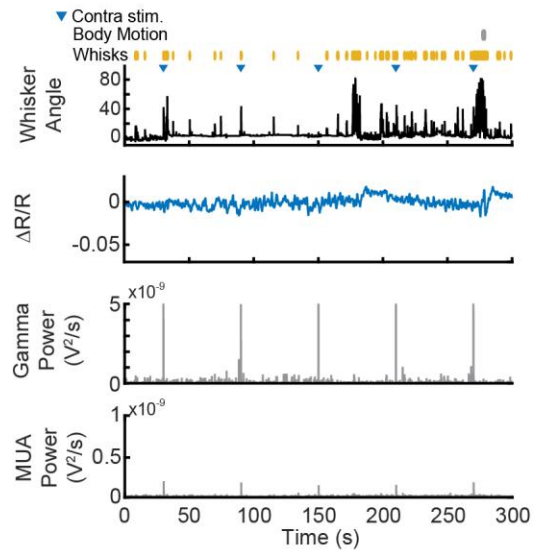
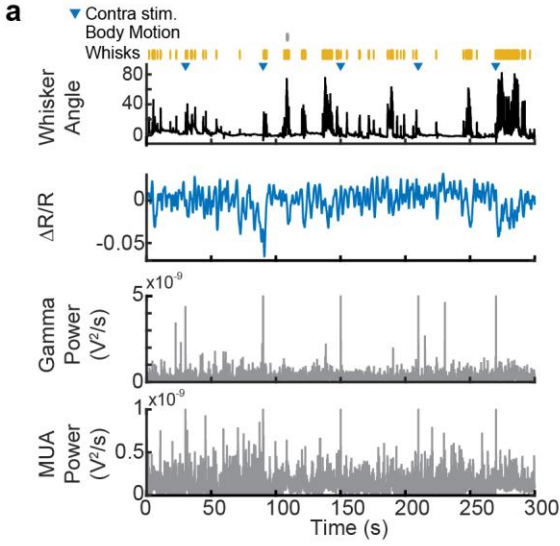


Supplementary Figure 8

Examples of the effects of pharmacological infusions on sensory-evoked and resting responses in individual animals

a: Top left: image of a thinned-skull window showing the locations of the CBV ROI (yellow shaded region), implanted cannula, and stereotrode scale bar = 1 mm. Top center: spatial map of the difference between the average aCSF and muscimol CBV responses to a contralateral whisker stimulus 0.5 to 2 seconds after stimulation. Top right: the spatial map of the difference between the standard

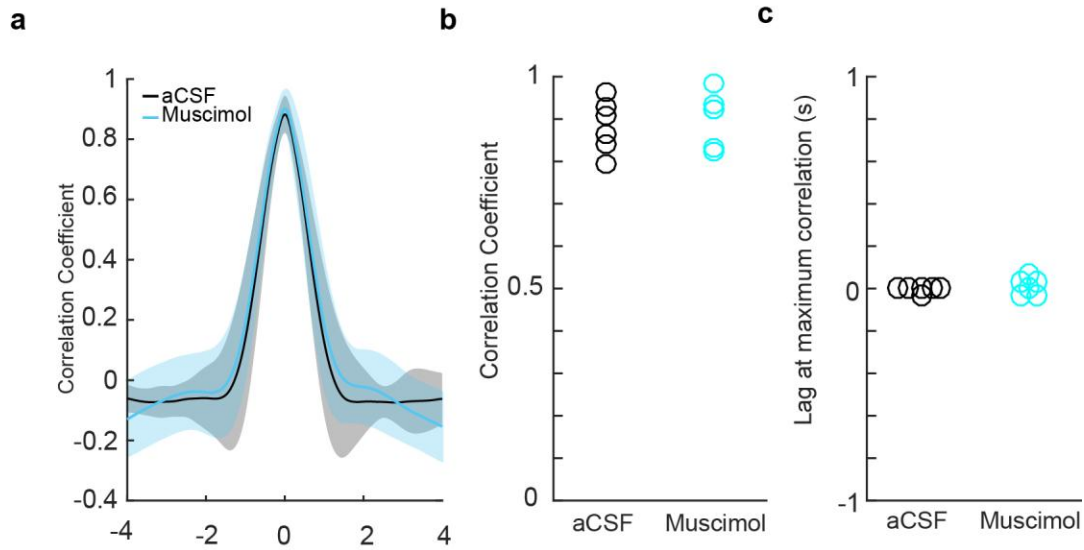
deviation of CBV at rest following aCSF and muscimol infusions. Bottom left: the average sensory evoked MUA power for the example animal compared between aCSF (black) and muscimol (blue) infusions (bottom left). Bottom right: two examples of the CBV measured during single periods of rest following aCSF (black) and muscimol (blue) infusions (bottom right). b,c: Same as a, but for an animal infused with muscimol+CNQX+AP5 and the muscimol+adrenergic blockers, respectively.



Supplementary Figure 9

Changes in sensory-evoked neural activity following infusion.

a: Example data from two representative trials following aCSF (left panel) and muscimol (right panel) infusions. Movement of the whiskers (orange tick marks) were detected from the whisker angle (top), movement of the body (gray tick marks) and stimulation times (blue triangles) were also tracked. Normalized reflectance changes were averaged over a region of interest within the thinned skull window (second from top). Gamma-band power (third from top) and MUA (bottom) following infusion. b,c: Same as a, but from different animals following muscimol+CNQX+AP5 and muscimol+adrenergic blocker infusions, respectively.



Supplementary Figure 10

CBV fluctuations after muscimol infusions do not propagate from nearby regions

a: Mean (solid line) and standard deviation (shaded region) of cross-correlograms between the reflectance within the region of interest and the reflectance from the rest of the window ($n=6$, three animals omitted which had windows that were spanned by the ROI). b: Comparison of the correlation coefficients between aCSF and muscimol infusions. The correlations were not significantly different (paired t-test, $p=0.12$, $t(5)=-1.9$). c: Comparison of the lags at maximum correlation between aCSF and muscimol infusions. The lags were not significantly different (paired t-test, $p=0.3$, $t(5)=-1.17$).